Drug/Bioactive Eluting Chitosan Composite Foams for Osteochondral Tissue Engineering

Muhammad Samie[1,2,3,4,5,*], Ather Farooq Khan[1], Saeed ur Rahman[6], Haffsah Iqbal[1], Muhammad Arfat Yameen[2], Aqif Anwar Chaudhry[1], Hanaa A. Galeb,[3,7] Nathan R. Halcovitch,[3] John G. Hardy[3,4,*]

[1] Interdisciplinary Research Centre in Biomedical Materials, COMSATS University Islamabad, Lahore campus, 54000, Pakistan.

[2] Department of Pharmacy, COMSATS University Islamabad, Abbottabad campus, 22060, Pakistan.

[3] Department of Chemistry, Lancaster University, Lancaster, Lancashire, LA1 4YB, United Kingdom.

[4] Materials Science Institute, Lancaster University, Lancaster, Lancashire, LA1 4YW, United Kingdom.

[5] Institute of Pharmaceutical Sciences, Khyber Medical University, Peshawar, Khyber Pakhtunkhwa, 25100, Pakistan.

[6] Institute of Basic Medical Sciences, Khyber Medical University, Peshawar, Khyber Pakhtunkhwa, 25100, Pakistan.

[7] Department of Chemistry, Science and Arts College, Rabigh Campus, King Abdulaziz University, 21577 Jeddah, Saudi Arabia.

Abstract

Joint defects associated with a variety of etiologies often extend deep into the subchondral bone leading to functional impairment and joint immobility, and it is a very challenging task to regenerate the bone-cartilage interface offering significant opportunities for biomaterial-based interventions to improve the quality of life of patients. Herein drug-/bioactive-loaded porous tissue scaffolds incorporating nano-hydroxyapatite (nHAp), chitosan (CS) and either hydroxypropyl methylcellulose (HPMC) or *Bombyx mori* silk fibroin (SF) are fabricated through freeze drying method as subchondral bone substitute. A combination of spectroscopy and microscopy (Fourier transform infrared (FTIR) spectroscopy, scanning electron microscopy (SEM), X-ray diffraction (XRD), energy dispersive X-ray (EDX), and X-ray fluorescence (XRF) were used to analyze the structure of the porous biomaterials. The compressive mechanical properties of these scaffolds are biomimetic of cancellous bone tissues and capable of releasing drugs/bioactives (exemplified with triamcinolone acetonide, TA, or transforming growth factor-β1, TGF-β1, respectively) over a period of days. Mouse preosteoblast MC3T3-E1 cells were observed to adhere and proliferate on the tissue scaffolds as confirmed by the cell attachment, live-dead assay and alamarBlue^{TM} assay. Interestingly, RT-qPCR analysis showed that the TA downregulated inflammatory biomarkers and upregulated the bone-specific biomarkers, suggesting such tissue scaffolds have long-term potential for clinical application.

Keywords

Chitosan; Composites; Osteogenesis.

1. Introduction:

Joints injuries are very common worldwide, particularly among athletes and ageing populations, caused by mechanical stress (sports injury, repetitive trauma etc.) or biological stress

(osteonecrosis, osteochondritis dissecans etc.) and often associated with swelling, pain and stiffness of the whole joint [1]. The progressive deterioration of the defect leads to the involvement of subchondral bone where the existence of an interface (osteochondral interface) between the two dissimilar tissues becomes the main hurdle in its healing/treatment. A variety of conservative treatments (commonly pain management medication) and surgical treatments exist (ranging from the orthobiologics to advanced arthroscopic techniques) to treat joint defects [2, 3]. Several studies have been conducted to compare various treatments and understand which is the best treatment option, however, failure in treatment was observed in many patients at later stages of life [4, 5], and there is therefore significant opportunity to improve long-term clinical outcomes [6-9].

The production of porous tissue scaffolds loaded with therapeutics (e.g., drugs, bioactives, etc.) to enhance osteoinduction and support self-healing is an exciting area of research in bone tissue engineering [10-14]. Both cellular and acellular scaffolds are used as templates to support the new tissue formation [15-19]. Tissue scaffolds with biomimetic microarchitectures/mechanics support the adhesion and proliferation of native cells and subsequent formation of the ECM [20-24]. Natural polymers (e.g., cellulose [25], CS [26], SF [27], alginates [28], and collagen [29]), synthetic polymers (e.g., polycaprolactone, polylactide, etc.) [30-33] and composites thereof [34-39] are employed in the production of biomaterials for bone tissue engineering. Previous treatment strategies were focused on the integration of the cartilage layer without considering the subchondral bone. However, successful integration of the osteochondral tissue requires the regeneration of the basal subchondral layer which is crucial for the cartilage formation.

The development of composite biomaterials for bone tissue engineering is an active area of biomaterials science and engineering [34, 35, 40-43]. Polymers are widely employed in biomaterials due to their useful properties, for example, CS has antibacterial properties [44], and

B. mori SF has pro-regenerative properties [45, 46], moreover both polymers can be processed into various morphologies like films, fibers, hydrogels, and foams/sponges alone and as composite materials with mechanics mimetic of the biological niche in which they may be used [47-49]. Such biomaterials may offer the biological/environmental factors that are instrumental to successful bone tissue engineering, with long term prospects for clinical application [50-53]. It is now well established that regeneration of the bottom layer is more important than the cartilage layer alone hence layered scaffolds have also gained attention to facilitate the regeneration of interfaces where different tissue types having different physiology are connected.

Inflammation at defect sites may facilitate healing by generating a pro-regenerative response, however, severe inflammatory responses arising after surgery may hinder/halt the regeneration, consequently, it is important to effectively manage inflammatory responses in tissue engineering [54-56]. Joint defects typically present elevated levels of tumor necrosis factor-α (TNF-α) and interleukins with inflamed synovium that downregulates extracellular matrix (ECM) production and the anabolic activity of the cells [57-59]. To reduce inflammation in joints, triamcinolone acetonide (TA) can be administered [60-64]; and site-specific delivery of drugs from biomaterials circumvents systemic pharmacokinetic challenges and off-target effects [65]. Scaffolds loaded with drugs/bioactives provide dual functionality in terms of local delivery of the payload in the extracellular environment, as well as serving as a support for the cells to organize in a 3D fashion [66-68]. Here we report the development of novel composite biomaterials loaded with either TA or TGF-β1, where the elution of the drug/bioactive payload from the scaffolds is intended to control the inflammatory response and enhance the osteogenic response, using the mouse MC3T3 preosteoblast cell line for *in vitro* validation of the approach.

2. Materials and methods

2.1. Materials

B. mori silk cocoons were procured from the Forestry Department at Changa Manga Forest Park (Lahore, Pakistan). CS (MW: 26200 & DDA: 90%) was obtained from Mian Scientific, Lahore, Pakistan. HPMC was received from VWR International Ltd, Lutterworth, Leicestershire, UK. TA was received as gift sample from Gean Pharmaceuticals (Sheikhupura Road, Lahore, Pakistan). Acetic acid, ethyl alcohol and methyl alcohol were purchased from DaeJung Chemicals & Metals (Gyeonggi-do, South Korea). Phosphate buffered saline (PBS) tablets (0.1M, pH 7.4), nHAp (Sintering grade < 200 nm particle size), dialysis membrane (MWCO 12kDa), paraformaldehyde (PFA), resazurin sodium salt cell culture grade (MW: 251.17g/mol), propidium iodide (PI) and 4′,6-diamidino-2-phenylindole dihydrochloride (DAPI) were purchased from Sigma-Aldrich (Steinheim am Albuch, Germany). Calcein AM (MW: 994.86) was purchased from AAT Bioquest (Pleasanton, CA, USA). Recombinant human TGF-β1 (Cat # 100-21) and human TGF-β1 pre-coated ELIZA kit (Cat # BGK01137) were purchased from PeproTech EC Ltd. (London, UK). Sodium carbonate (anhydrous) was purchased from Scharlab S.L (Barcelona, Spain). The mouse MC3T3 preosteoblast cell line (ATCC # CRL-2593TM) was obtained from the American type culture collection (ATCC) global resource center (Manassas, VA, USA). 10% Foetal Bovine Serum and 1% penicillin and streptomycin were purchased from Caisson, USA. TRIzol® Reagent (Cat # 15596026) and lithium bromide, Minimum essential medium (α-MEM), trypsin-EDTA and cell culture grade PBS from Gibco®, by Life Technologies™, were procured from ThermoFisher Scientific (Waltham, MA, USA). Protoscript® First strand cDNA synthesis kit (Cat # E600L) was obtained from New England Biolabs Inc. (Ipswich, MA, USA). Real time PCR reagents, synthesized primers and probes for GAPDH were obtained from Macrogen (Seoul, South Korea).

Trypan blue was purchased from ACI Chemicals Ltd. (Dhaka, Bangladesh). All chemicals were either used as received and stored in line with the supplier's recommendations.

2.2. Preparation of porous composite foam tissue scaffolds

Porous composite foam tissue scaffolds with variable amounts of the polymers (i.e., SF, CS, HPMC) and nHAp were prepared by freeze drying (an adaptation of our previously reported protocol [69]. Briefly, a 2% acetic acid solution was used to dissolve CS (typically taking 4-6h) at room temp, yielding a 33 wt% aqueous CS solution; nHAp was added to this solution with the help of an ultrasonicator to form a uniformly dispersed slurry. A solution of SF denaturant was prepared by dissolution of anhydrous calcium chloride (111 g, 1 mole) in distilled water (144 g, 144 mL, 8 moles), and to this solution ethanol (92.1 g, 116.8 mL, 2 moles) was added; 50 mL of this solution was used to dissolve 15 g of SF by stirring at 80°C for 1 hr., followed by filtration over a glass frit and dialysis (MWCO 12kDa) against concentrated PEG solution for 48 hrs., in accordance with the literature [70]. Optionally both the CS and SF solutions were mixed as required and crosslinking was induced as a result of hydrogen bonding by the addition of HPMC, along with: unloaded TA, TA loaded polycaprolactone microspheres (prepared according to a reported literature protocol for providing prolong release of the drug from scaffolds [71], drug loading in polycaprolactone microspheres was determined by UV-vis spectroscopy, and observed to be 28% by weight; on the basis of this data, the microspheres were added to the scaffolds (i.e., 5% drug and 18% PCL by weight; sample B3 in Table 1)) and/or TGF-β1; the slurries were transferred into molds and stored overnight at -40°C prior to lyophilization for 48h to obtain the porous composite tissue scaffolds. The precise compositions of the biomaterials in their dry state are shown in **Table 1**. The control composite scaffolds (B1) were fabricated using the same preparation method without the addition of drugs. The addition of microspheres into the scaffolds

was also performed by a post seeding method rather than in situ loading, where the microspheres were dispersed in deionized water and added to the surface of tissue scaffolds where both gravitational force and flow of liquid across the pores led to the distribution of microspheres on the polymeric surfaces inside the tissue scaffolds.

2.3. Scanning electron microscopy (SEM) and energy dispersive X-ray (EDX) spectroscopy

SEM images and EDX spectra were recorded using a Tescan VEGA3 equipped with EDX (Brno - Kohoutovice, Czech Republic). Rectangular blocks of the scaffolds after gold sputtering were analyzed for microstructure and elemental distribution, and further processed using Fiji ImageJ.

2.4. Fourier transform infrared (FTIR) spectroscopy

FTIR spectra were recorded using ThermoFisher scientific FTIR (Nicolet-6700^{TM}, USA) coupled with an attenuated total reflectance (ATR) accessory in the spectral region of 650-4000 cm^{-1} at room temperature. The analysis was carried out at a resolution of 8 cm^{-1} accumulating a total of 128 number of scans per sample.

2.5. X-ray diffraction (XRD) analysis

X-ray diffractograms were collected using a Rigaku Smartlab powder diffractometer (Rigaku Ltd., Kent, UK) equipped with a DTex250 one-dimensional (1D) detector, irradiating the films at a wavelength of 0.15418 nm, from Cu K radiation. The Cu source was operated at 45 kV and 200 mA, and was fitted with parallel beam optics, with a scan range of 2Θ = 5–60°.

2.6. X-ray fluorescence (XRF) analysis

X-ray fluorescence measurements were performed on a Shimadzu EDX-8000 instrument. The samples were gently crushed using a stainless-steel spatula and placed on a thin film of Mylar, and irradiated with a beam of 0.5mm radius. The counting time was 180 seconds and the elemental intensities were analyzed using the Fundamental Parameter (FP) method. No balance medium was used in the analysis, and so only elements above 0.5 weight % in the final output are considered. Interpretation of these weight % is only qualitative but confirms the presence of Ca and P, with possible contaminants of Si and S. However, it is noted that Si and S are often contaminants of the Mylar film used to mount the samples.

2.7. Swelling ratio analysis

The swelling ratio of a tissue scaffold (i.e., its capacity to absorb water after immersion in PBS solution (pH 7.4) at 37 ± 0.5°C) for different time intervals was recorded (n=3). The dry weight (W_d) of the scaffolds was recorded before immersion of the scaffolds in PBS after which it was stored, then blotted on paper before recording the wet (W_s) weight of the blotted samples. The % water uptake was calculated using the following formula:

$$\%\ \text{Water uptake} = W_s - W_d / W_d \times 100$$

2.8. Degradation testing via mass loss

Degradation of the composite scaffolds was determined by immersion of a pre-weighed sample (n=3) (W_0) in PBS (pH 7.4) maintained at 37°C for various time intervals. At the end of every time point the samples were removed from the medium, dried in an oven at 65°C overnight and their weight was again recorded as W_1. The percent degradation was then calculated using the following formula:

$$\% \text{ Degradation} = W_o - W_1/W_o \times 100$$

2.9. Porosity testing

A liquid displacement method employing ethanol as the displacement solvent was used to find out the porosity of composite scaffolds. For this purpose, a pre-weighed sample was immersed in a known volume (V_1) of ethanol in a graduated cylinder (n=3). The final volume with scaffold was noted as V_2 and after removal of the sample the final volume was recorded as V_3. The porosity was calculated using the following formula:

$$\% \text{ Porosity} = V_1 - V_3/V_2 - V_3 \times 100$$

2.10. Mechanical testing

Mechanical testing of samples (n=3) was carried out at room temperature in accordance with the ASTM D5024-95a guidelines. An electrodynamic fatigue testing machine (LFV-E 1.5kN) with a load cell of 1.5kN was used to compress the rectangular scaffold blocks having dimensions of (5x3x3mm) at a strain rate of $1x10^{-3}$/s, and crosshead speed between 0.2-0.35mm/min up to 25% deformation. The obtained results were used to calculate mean elastic modulus and universal compressive strength.

2.11. *In vitro* drug release studies and release kinetics

To carry out the drug release studies, scaffolds measuring an equal amount of drug were added into 10 mL PBS solution maintained at 37 ± 0.5°C in a water bath (n=3). At predetermined time intervals an aliquot volume approximating 1 mL was withdrawn, filtered and analyzed to quantify the amount of released drug, i.e., TA at a wavelength of 236 nm using UV-vis spectrophotometer and TGF-β1 at 490 nm using ELIZA kit following the manufacturer's specification with the help of a microplate reader (Bio-Rad PR4100). After each withdrawal an equal volume of pre-warmed

fresh PBS was added/replenished to keep the sink conditions constant. From the data obtained, the cumulative drug release was then calculated. Afterward the data was fitted into various kinetic models to study the release pattern from the matrices.

2.12. Cell culture

Mouse MC3T3-E1 pre-osteoblast cells were cultured using fresh medium supplemented with the requisite ingredients. Cells of passage (P=5) were trypsinized with trypsin/EDTA before seeding and incubated at 37°C in a 5% CO_2 incubator. Cells from fresh culture were seeded on pre-sterilized scaffolds (Gamma radiated at a dose of 2.5 K Grey) (n=3) and incubated in a 5**%** CO_2 incubator.

2.12.1. Cell attachment assay

To study the behavior of cells towards the scaffolds an adhesion/attachment assay was performed. Exponentially growing cells at a density of $2x10^4$ cells/well were seeded on the scaffolds in a 24 well plate. The samples after incubation for 3-days in a 5% CO_2 incubator at 37°C were washed thoroughly with cell culture grade PBS and fixed with 4% PFA solution for 30 min, followed by dehydration using a serial dilution (50%, 60%, 70%, 80%, 90% and 100%) of ethanol. The samples after air drying were analyzed via SEM.

2.12.2. Cell viability and proliferation assay

2.12.2.1. alamarBlue™ assay

A nondestructive alamarBlue™ assay was carried out to quantitatively measure cell viability. Exponentially growing cells at a density of $2x10^4$ cells per well were aseptically seeded onto the scaffolds in a 24 well plate and incubated at 37°C for specified time points (i.e., 2 & 8 days) in a 5% CO_2 incubator. 200 µL of alamarBlue™ working standard was added to each well containing 2 mL of cell culture medium after specified periods. The samples were again incubated for 4-5 h

in the dark inside a 5% CO_2 incubator. Bio-Rad PR4100 absorbance microplate reader was then used to measure absorbance at a wavelength of 550 and 620nm. Cells grown on tissue culture plates were used as a positive control.

2.12.2.2. Live/dead assay

Samples incubated with MC3T3 preosteoblast cells at 37°C in a 24 well plate for 9 days in a 5% CO_2 incubator were estimated for number of live and dead cells. The assay was carried out by careful aspiration of the growth medium and incubation of the samples with 3µM Calcein AM and 2.5-5µM propidium iodide in DPBS for 30 min in dark. 400 µL of this solution was added into each well of 24 well plate and were observed using fluorescence microscope supplied with green and red filters. The obtained images were further processed in Fiji ImageJ.

2.12.3. RT-qPCR

The gene expression analysis of the TA loaded scaffolds was carried out in accordance to a previously established protocol [72] using real-time quantitative PCR (Qiagen Rotor-Gene® Q 5Plex HRM) provided with 2.3.5 software from the manufacturer. Briefly, the MC3T3 cells after interaction with the scaffolds for 12h were lysed using Trizol reagent to isolate RNA. The isolated RNA was quantified using nanodrop and used to synthesize cDNA library according to the manufacturer's protocol. The transcription level of four genes including TNF-α, IL-6, RUNX2 & ALP were quantified according to the reference gene GAPDH with the help of SYBR green dye. The primer sequences of mouse genes used in the study are given in **Table 2**.

2.13. Statistical analysis

Each sample data represents triplicate run (n=3) as the mean ± standard deviation (SD). Analysis was performed using GraphPad Prism-8 software. One-way analysis of variance (ANOVA)

statistics followed by Post hoc Dunnett test was used. p-value ≤ 0.05 was considered as statistically significant.

3. Results and Discussion

3.1. Scaffold preparation and microscopic and compositional analysis

The porous composite tissue scaffolds were prepared by a simple, scalable freeze-drying method (depicted in **Scheme 1**), with their compositions clarified in **Table 1**. Surface characteristics of a biomaterials play an important role in their interactions with the external environment. The SEM images of the porous composite scaffolds as displayed in **Figure 1** show the pore walls to have both smooth and rough surfaces due to the presence of the various polymeric/particulate components in the composites in line with the literature [73]. The mean pore diameter of the scaffold was found to be 64 ± 1.06 µm. An interconnected and stratified 3D porous structure with both micropores and macropores can be seen in the cross-sectional images which is supportive of cell migration/infiltration and nutrient/waste transport/diffusion. The overall porosity of the scaffolds remained $\geq 60\%$ in all samples, in line with the porosity measurement data obtained from liquid infiltration. A uniform distribution of the nHAp crystals in the form of white beads in the pore walls (highlighted by yellow arrow heads) (**Figure 1)**, as confirmed by EDX analysis. Moreover, uniformly distributed microspheres can be seen embedded in the polymeric matrices (highlighted by blue arrow heads), which suggests that in situ loading of microspheres could be an optimum method as compared to the post seeding method (where the microspheres were not well integrated in the polymeric matrix of the porous scaffolds). Interestingly, the distribution of microspheres inside the scaffolds using the post seeding technique was correlated to the size of the microspheres, and if the size of microspheres was less than pore size they infiltrated the scaffolds otherwise they sat on top of the scaffolds [74]. It was found that the type and ratio of polymers

affects the surface characteristics, i.e., the SF based scaffolds (**Figure 1: B4, B7 & B8**) had a smooth surface, whereas the CS-based scaffolds (**Figure 1: B1-B3, B5 & B6**) had rough surfaces which is in line with the literature [75].

Elemental analysis of the composite scaffolds was assessed via EDX analysis (**Figure 2**). Peaks at values of 0.3, 0.38, 0.6, 2.1 and 3.7 KeV were observed for both CS-based and SF-based tissue scaffolds. The peaks both at 0.38 and 3.7 KeV are characteristic of Ca^{2+}, and the peak at 2.1 KeV is characteristic of P in PO_4^{3-}, thereby confirming the nHAp is present in the scaffolds in line with the literature [76]. The peaks at 0.3 and 0.6 are the representative peaks of C and O which are present in the polymeric components (CS/SF/HPMC) in the samples. In case of SF-based tissue scaffolds another peak pointing at 1.15 KeV is characteristic of Na as a trace residue from PBS. Complementary elemental analysis via XRF (**Table 1**) confirmed the presence of Ca and P in all samples.

3.2. FTIR analysis

The FTIR spectra of unloaded, TA-loaded and TGF-β1-loaded scaffolds (B1-B8) are shown in **Figure 3** whereas the individual components are shown in **Figure 4**. The spectra of B1-B3 shows all the characteristic peaks for CS and/or HPMC; i.e., the peak at 1046 cm^{-1} is characteristic of the C-O-C stretching of glucosamine residues, whereas the peaks at 1420 cm^{-1}, 1550 cm^{-1} and 1680 cm^{-1} are characteristic of the C=O stretching of the amide bond and N-H of the amino group of CS [77]. As both CS and HPMC are polysaccharides and have similar structures, the bands overlap each other. A slight change in peak intensity and position is characteristic of new non-covalent interactions, most likely hydrogen bonds [78], and peaks between 1420 cm^{-1} and 1680 cm^{-1} in case of B2 and B3 may arise from the drug (TA).

In the SF-based scaffolds, the absorptions at 1611 cm^{-1}, 1507 cm^{-1} and 1224 cm^{-1} arise from the amide I (C=O stretching), amide II (C≡N stretching) and amide III bands, respectively. A slight change in peak intensity and shift from 1611 cm^{-1} to 1620 cm^{-1} for the amide I (characteristic of the presence of β-sheets), and 1224 cm^{-1} to 1240 cm^{-1} for the amide III were seen in the scaffolds B4, B7 and B8. These slight changes may be a result of the intermolecular interaction of the polypeptide chain with the solvent altering the degree of crystallinity and/or intermolecular/intramolecular hydrogen bonding between polypeptide chains (e.g., β-sheet formation, however, complex composites containing more than one biopolymer with amides makes this difficult to quantify). The nHAp exhibit typical non-degenerating symmetric stretching of P=O bond at 950 cm^{-1}, and degenerated asymmetric stretching of P-O bond appears at 1060 cm^{-1} and 1015 cm^{-1}, respectively [79]. The appearance of peaks between 1338 cm^{-1} and 1473 cm^{-1} can also be seen in the scaffolds B4, B7 and B8. The broad peak in the range of 3000 cm^{-1} – 3600 cm^{-1} was common in almost all scaffolds which corresponds to the overlapping of free hydroxyl group and stretching vibrations of N-H of amino group from CS and HPMC. It can be seen that the addition of TGF-β1 into these scaffolds had no observable effect on the scaffolds.

3.3. XRD analysis

Figure 5 displays the XRD patterns of the various scaffolds. XRD data for samples with CS showed characteristic broad peaks at ca. $2\theta \approx 10°$ and 20°; XRD data for samples with HPMC showed the characteristic broad peak at ca. $2\theta \approx 20°$; XRD data for samples with SF were largely amorphous (broad peak at $2\theta \approx 20°$), with evidence of crystalline content (peaks at $2\theta = 19.9°$ and 24.0°) suggesting β-sheet content in line with FTIR measurements; the characteristic peaks for nHAp (at $2\theta = 31.8°$, 32.6°, 32.9° and 33.1°) are evident in most XRD patterns albeit somewhat obscured in the samples containing SF.

3.4. Swelling analysis

Ability of biomaterials to absorb water and retain its structure is important for its function as a tissue scaffold. Swelling depends on the internal crosslinking of the polymers and the greater the degree of crosslinking, the less swelling, and vice versa. **Figure 6** shows the swelling behavior of all scaffolds after a 24 h period in PBS. It can be seen that the SF-based scaffolds i.e., B4 and B8 exhibited less swelling (i.e., 4.73 ± 0.03% and 4.54 ± 0.31%, respectively), than the CS/HPMC-based scaffolds. This difference in the swelling of SF-based scaffolds is in part due to the intermolecular interactions between the protein chains lacking between the polysaccharides CS and HPMC [80]. Another factor affecting water uptake is the degree of porosity, as the porous structure can hold large volumes of liquid within the empty spaces.

In the case of B7, a slight increase (5.37 ± 0.24%) in swelling was seen which can be again attributed to the addition of CS to the SF solution. the β-sheet content of SF influences water solubility, thereby reducing swelling and slowing degradation, while concomitantly increasing mechanical properties [81]. A very minor difference in the swelling of B5 and B6 was noted (i.e., 7.23 ± 0.04% and 7.83 ± 0.12%, respectively). The highest values for swelling ratio with an increasing order were noted for B3 < B1 < B2, with values of 8.44 ± 0.38%, 8.55 ± 0.16% and 8.62 ± 0.21%, respectively. Increased liquid uptake facilitates transport of nutrients and waste to/from resident cells, whereas, increased swelling ratio slows cell infiltration within the scaffold. the addition of the ceramic (nHAp) to the scaffolds was observed to reduce the swelling ratio which is in accordance with the literature [82]. These results show that SF-based scaffolds exhibit the optimum swelling behavior which is useful for tissue engineering.

3.5. Degradation analysis

Degradation assessed by the percentage weight loss over time was analyzed with a view to understanding prospects for successful integration of the scaffolds into native tissues. If a scaffold degrades at a very slow rate that may impede ingrowth of new tissue, whereas if it degrades too quickly it may not offer mechanical support for long enough. Ideally the degradation rate of the scaffold should coincide with the formation of native tissue which is dependent on the type and location of the defect [83]. Consequently, time dependent degradation of the scaffolds was analyzed at five different time points (i.e., day 1, day 3, day 7, day 10 and day 14), with representative results for day 1 & 14 shown in **Figure 7** (a complete set of data is presented in the supplementary information, **Figure S1**). Degradation of the scaffolds starts on day 1 and carries on over the course of the experiment. The rate of degradation of B5 was significant (i.e., 5.2 ± 0.3% ($p<0.01$)) after day 1 when compared to the control B1. Non-significant weight loss as compared to B1 was exhibited by composites B2, B3, B6 and B7 after day 1 (having values of 4.5 ± 0.3%, 3.5 ± 0.3%, 4.1 ± 0.2% and 4.4 ± 0.3%, respectively); significantly less degradation loss was noted for composites B4 and B8 (2.0 ± 0.2% and 2.1 ± 0.4% weight loss, respectively).

Weight loss continued with time for all composites as compared to B1 (control) with different rates. The non-significant difference in degradation of the scaffolds after the addition of TA or TA-loaded microspheres became significant after day 14, but for composite B2 it increased in rate, and for composite B3 it decreased in rate, relative to the control. For all other composites a similar trend was seen after each time point. The percent degradation of the composites after 14 days of incubation in the medium in increasing order was B4 < B8 < B7 < B3 < B1 < B6 <B2 < B5 (with experimental values 10.1 ± 0.3%, 10.4 ± 0.4%, 13.6 ± 0.2%, 16.9 ± 0.4%, 18.7 ± 0.4%, 19.8 ± 0.4%, 20.0 ± 0.2% and 20.7 ± 0.2%, respectively). It can be seen that the CS-based scaffolds

exhibited a total weight loss of around 20%, whereas SF-based scaffolds showed ca. 10% weight loss, suggesting the SF-based scaffolds would degrade more slowly than CS-based scaffolds.

3.6. Porosity analysis

Porosity is very important as the highly porous structure facilitates cells infiltration which in turn compromises the mechanical properties of the scaffold. It has been previously suggested that a scaffold for bone tissue regeneration should have a porosity of more than 60% [24, 84, 85]. Scaffold porosity determined by solvent displacement (**Figure 8**) shows the composites have similar porosities. The unloaded scaffold (B1) used as a control had a porosity of 65.7 ± 2.1%. Addition of drug to the composite (B2) has resulted in increased porosity with value of 68.8 ± 1.3%, whereas addition of TA-loaded microspheres to composite (B3) resulted in non-significant decrease ($p>0.05$) in porosity as compared to the control (62.0 ± 1.0%).

The addition of TGF-β1 to the scaffolds has no effect on the porosity as can be seen from the porosity data of composite B1, B5 and B6 with values 65.8 ± 2.1%, 66.8 ± 3.6 and 65.6 ± 0.6% respectively. A significant increase in porosity was observed for composites B4 and B8 (80.3 ± 1.8% ($p<0.0001$) and 77.0 ± 1.4% ($p<0.001$), respectively). The highly porous structure is beneficial for tissue engineering in terms of cell transplantation and cultivation [86], and the presence of SF encourages highly porous structures through freeze drying (which plays a role in β-sheet formation) [87]. Porosity is linked to the mechanical properties of materials, however, the irregular pore shapes/sizes in the composite scaffolds described herein make it illogical to attempt to draw conclusions about correlation between porosity and mechanics which are important for their success [88].

3.7. Mechanical properties

Mechanical properties play a pivotal role in the effective design of tissue scaffolds for tissue regeneration, wherein biomaterials with biomimetic properties are desirable [89], composite materials can be prepared where the ratio of components control the mechanical properties of the biomaterials [90, 91]. The compressive properties of the biomaterials studied herein were observed to be of a similar order of magnitude (low MPa regime) to natural human tissue (e.g., soft bone tissue, cartilage tissue, etc. [92, 93]) as shown in **Figure 9**. The elastic modulus of B1, B2 and B3 was found to be 3.17 ± 0.04 MPa, 3.11 ± 0.09 MPa and 3.70 ± 0.28 MPa, respectively. The compressive strength of B1 was 0.21 ± 0.02 MPa and B2 was 0.27 ± 0.02 MPa, showing a statistically non-significant difference ($p \geq 0.05$); however, a significant difference was seen when comparing to B3 and B6 which have values of 0.31 ± 0.03 MPa ($p=0.0084$) and 0.32 ± 0.03 MPa ($p=0.0063$), respectively. Both the elastic modulus and compressive strength was significantly higher ($p<0.0001$) for composites B4, B5, B7 and B8. The elastic modulus values were 4.67 ± 0.19 MPa, 4.84 ± 0.21 MPa, 3.98 ± 0.13 MPa and 4.98 ± 0.12 MPa, whereas the compressive strength values were 0.81 ± 0.06 MPa, 0.83 ± 0.01 MPa, 0.73 ± 0.03 MPa and 0.85 ± 0.05 MPa respectively. Composite B6 was observed to have the most significant increase in both elastic modulus and mechanical strength (3.84 ± 0.24 MPa and 0.32 ± 0.03 MPa ($p=0.0063$), respectively). Interestingly, the SF-based tissue scaffolds showed greater increases in mechanical strength than CS-based tissue scaffolds, potentially because of its propensity for intermolecular and intramolecular interactions (e.g., β-sheet formation).

3.8. *In vitro* drug release studies and release kinetics

The cumulative release data of both TA and TGF-β1 from the respectively loaded scaffolds (B2, B3 & B5-B8) shows release from the matrices over the period of 72 hours (**Figure 10**). The release

of TA from B2 is greater than B3, and this is observed to increase over time because of the incorporation of the drug inside microspheres in the case of B3 (consequently the drug has to diffuse through the polymer matrix into the sink medium), the release of the drug followed a concentration dependent mechanism and was affected by the degradation of the polymer along with the diffusion mechanism; the composites released 5.2 ± 1.3% and 2.7 ± 1.8% of the drug, respectively, after 2h in the release medium. A clear decline in the release rate of both composites can be seen after 12 h and the bend in curve has continued towards x-axis along with time; the composites released 70.6 ± 4.9% and 52.4 ± 2.3% of drug after 72 h, respectively.

By comparison with the release of TA, the release of TGF-β1 from composites (B5-B7) was slower, with a gradual increase after 24 h incubation. The only composite that has shown a slow and prolonged release among the TGF-β1-loaded scaffolds was B8. The mathematical values of cumulative TGF-β1 released from composites B5, B6, B7 and B8 was 23.19 ± 0.99%, 20.38 ± 0.88%, 19.20 ± 0.67% and 15.13 ± 1.88%, respectively. The cumulative release after 72 h was in the order B8 (40.28 ± 0.60%) < B7 (67.48 ± 2.02%) < B5 (76.32 ± 1.70%) < B6 (82.42 ± 4.78%), which shows that the SF-based scaffolds have the ability to prolong the release of the drug more than CS/HPMC-based scaffolds (correlating to the degradation studies). A concentration independent release mechanism following both dissolution and diffusion process was exhibited by the composite scaffolds (a complete set of data for drug release kinetics is presented in the supplementary information, **Table S1**).

3.9. Cell culture

3.9.1. Cell attachment assay

Adhesion of the cells on any surface is important for tissue scaffolds, and the attachment behavior of mouse MC3T3 preosteoblast cells after 3 days of culture on the scaffolds was studied (**Figure**

11). The cytoplasmic extensions from the cells (highlighted by the yellow arrows) secured the cells on the surface of the biomaterials. The attachment of cells only on the surface of a scaffold and forming a scar tissue layer at its surface limits the infiltration of cells within the scaffolds, resulting in rejection of the graft as a mechanically non-functional necrotic tissue; from the SEM results it is evident that the cells have effectively infiltrated the pores in the biomaterials (evidenced by formation of active and randomly distributed cytoskeletal extensions). The blue arrow heads are indicative of areas of the scaffolds with onset/observable degradation over time which is beneficial for the success of an implanted scaffold. No effect of the addition of TA or TGF-β1 on cell adhesion.

3.9.2. Cell viability and proliferation assay

3.9.2.1. alamarBlue™ (Resazurin) assay

The metabolic activity of a cell is the primary marker to estimate its viability. **Figure 12** shows bar graphs of cells on scaffolds at two different time points (i.e., at day 2 and day 8) against the positive control (i.e., tissue culture plastic, TCP). On day 2, a significantly reduced viability ($p<0.001$) can be seen for samples B1, B2, B3 and B6 (83.5 ± 2.0%, 81.9 ± 2.2%, 91.5 ± 1.5% and 84.4 ± 2.6%, respectively); however, the other samples had comparable viability to the control (non-significant difference, $p\geq0.05$, attributed to the presence of SF). By comparison, after 8 days of incubation all of the samples have shown either non-significant ($p\geq0.05$) difference in viability or significantly ($p<0.001$) improved viability as compared to the control. This clearly shows that the number of viable cells has been increased over time and resulted in enhanced metabolic activity. The scaffolds with significantly improved cell viability were B4, B5 and B8, which had values of 109.9 ± 2.2% ($p=0.0101$), 110.2 ± 2.3% ($p=0.0079$) and 112.2 ± 3.3% ($p=0.0016$),

respectively. Reduced metabolic activity is an early indicator of poor cell health that may result in compromised cell membrane integrity causing cell death.

3.9.2.2. Live/dead assay

Figure 13 shows the result of the live/dead assay of the mouse MC3T3 preosteoblast cells cultured on the scaffolds after 3 days of incubation. It is the cell membrane integrity that is used as the base for the Live/Dead assay, rather the metabolic activity of the cells that reduces the resazurin dye. It is evident form the images that viable cells (stained with green color) were present in each sample, whereas very few dead cells (stained red) were observed in the images which clearly shows the biocompatible nature of the developed scaffolds.

3.9.3. RT-qPCR

The severity of inflammation at the defect site strongly depends on the expression or suppression of the inflammatory markers. Herein the mRNA transcript expression level using real-time PCR after 24 h culturing of the samples with MC3T3 mouse preosteoblast cell line was studied, using four targets: TNF-α and IL-6 (inflammatory markers, **Figure 14**) and RUNX2 and ALP (bone markers, **Figure 15**). Composites B2 and B3 containing the anti-inflammatory drug (TA) have significantly ($p<0.05$) down regulated the target proteins. A 10-fold reduction in the expression of TNF-α can be seen in case of B2, compared to B3 where the fold decrease is 6; this difference in gene suppression is because of the incorporation of drug directly into scaffolds in case of B2 as compared to B3 (where the incorporated drug is included in the form of microspheres and the drug needs to elute from the microspheres). Similarly, a 10-fold decrease in the expression of IL-6 can be seen for both B2 and B3, which is significantly ($p<0.05$) lower than the control (B1). These results are showing a significant difference in the down regulation of target proteins by the

composites hence suggesting an anti-inflammatory potential of the scaffolds if implanted in an animal model.

In addition to the anti-inflammatory potential, the osteogenic potential of the same scaffold composites i.e., B2 and B3 was evaluated by quantifying the mRNA transcript level of two bone markers. B2 was observed to have a 10-fold increase, whereas B3 had a 9-fold increase in the upregulation of RUNX2 as compared to the control (B1) which is statistically significant ($p<0.05$). There is a small fold increase (i.e., 2.5 and 3-fold) for upregulation of ALP by sample B2 and B3 respectively.

Conclusion

Tissue scaffolds incorporating CS, nHAp and either HPMC or SF were prepared by a simple freeze-drying method, and microscopy and spectroscopy showed the components to be distributed evenly through the matrix of the porous tissue scaffolds. The tissue scaffolds had biomimetic mechanical properties suitable for trabecular/spongy bone tissue. The drug release data showed that loaded drugs and growth factor were released at a controlled rate instead of burst release which might be helpful in reducing the administration of postsurgical medication, and a reduction in release rate can be achieved through incorporation of the drug and/or growth factor inside microspheres. The cytocompatibility of the tissue scaffolds was shown by cell adhesion and viability tests, and PCR data demonstrated that the addition of anti-inflammatory drug can reduce the chances of inflammation at the defect site, and pro-osteogenic activity can be enhanced by the incorporation of both TGF-β1 and TA in the tissue scaffolds. On the basis of the results presented, we conclude such biomaterials have long-term potential for clinical applications in the field of subchondral tissue regeneration.

Future Prospects

The work presented in this study is part of an ongoing project which is going to be extended to the development of bilayered scaffolds for osteochondral regeneration and their *in vivo* evaluation using a small mammal (e.g., rabbit) model.

Acknowledgements

A.F.K. acknowledges financial support from the Pakistan Higher Education Commission (HEC) under the National Research Program for Universities (NRPU) project scheme (Grant No. 4099), M.S. and J.G.H acknowledge financial support from the International Research Support Initiative Program (IRSIP), and JGH acknowledges financial support from Lancaster University's Early Career Internal Grant Scheme. We thank the Ministry of Education of Saudi Arabia and the Saudi Cultural Bureau for financial support for H.A.G. (Grant: KAU1526).

Conflict of Interest

The authors declare no conflict of interest.

Data Availability Statement

The data that support the findings of this study are available from the corresponding author upon reasonable request.

Table 1. Composition of the composite tissue scaffolds.

Composite	Code	HPMC (%)	CS (%)	nHAp (%)	SF (%)	TA (%)	TGF-β1 (µg)	PCL (%)	Ca by XRF (%)	P by XRF (%)
CS/HPMC/nHAp	B1	25	33	42	-	-	-	-	82.3	16.7
CS/HPMC/nHAp/TA	B2	25	30	40	-	5	-	-	84.5	14.9
CS/HPMC/nHAp/TA MS	B3	20	30	27	-	5	-	18	85.0	14.2
SF/nHAp	B4	-	-	25	75	-	-	-	82.1	8.2
CS/nHAp/TGF	B5	-	80	20	-	-	1.5	-	82.0	17.8
CS/HPMC/nHAp/TGF	B6	25	33	42	-	-	1.5	-	81.6	17.9
CS/SF/nHAp/TGF	B7	-	45	20	35	-	1.5	-	81.1	15.0
SF/nHAp/TGF	B8	-	-	20	80	-	1.5	-	81.9	10.6

Table 2. Primer sequence used in the RT-qPCR analysis

Gene	5'- 3'	Primer
GAPDH	Forward	AGG TCG GTG TGA ACG GAT TTG (21mer)
	Reverse	TGT AGA CCA TGT AGT TGA GGT CA (23mer)
TNF-α	Forward	CTG AAC TTC GGG GTG ATC GG (20mer)
	Reverse	GGC TTG TCA CTC GAA TTT TGA GA (23mer)
IL-6	Forward	GGA ATT CGT GGA AAT GAG AA (20mer)
	Reverse	GCA CTA GGA AAG CCG AGT AC (20mer)
RUNX2	Forward	GAC CAA AGT CAG TGA GT (20mer)
	Reverse	CCC AGT CCC TGT TTT AGT TGT AC (23mer)
ALP	Forward	CTA CGC ACC CTG TTC TGA GG (20mer)
	Reverse	GGA AGT TGC CTG GAC CTC TC (20mer)

Figure Captions/Legends

Scheme 1. Porous tissue scaffold preparation.

Figure 1. SEM micrographs of the composite scaffolds (B1-B8). Yellow arrows indicate nHAp, blue arrows indicate microspheres.

Figure 2. Representative EDX spectra. Left) CS-based scaffolds. Right) SF-based scaffolds.

Figure 3. FTIR spectra of the unloaded, TA-loaded and TGF-β1-loaded composites (B1-B8).

Figure 4. FTIR spectra of the individual components of the scaffolds.

Figure 5. XRD patterns of the scaffolds.

Figure 6. Swelling ratio of the unloaded, TA loaded and TGF-β1 loaded composite scaffolds (B1-B8) after 24 h incubation. Mean ± SD (n=3), *p<0.05, **p<0.01, ***p<0.001, ****p<0.0001.

Figure 7. Degradation behavior of the unloaded, TA loaded and TGF-β1 loaded bottom layer composite scaffolds (B1-B8). Mean ± SD (n=3), *p<0.05, **p<0.01, ***p<0.001, ****p<0.0001.

Figure 8. Percent porosity of the unloaded, TA loaded and TGF-β1 loaded composite scaffold composites (B1-B8). Mean ± SD (n=3), *p<0.05, **p<0.01, ***p<0.001, ****p<0.0001.

Figure 9. Mechanical properties of the unloaded, TA loaded and TGF-β1 loaded bottom layer composite scaffolds (B1-B8). Mean ± SD (n=3), *p<0.05, **p<0.01, ***p<0.001, ****p<0.0001.

Figure 10. Cumulative drug release behavior from composite tissue scaffolds. TA-loaded scaffolds (B2-B3) and TGF-β1-loaded composites (B5-B8). Mean ± SD (n=3).

Figure 11. SEM images MC3T3 pre-osteoblast cells on the composite tissue scaffolds. Yellow arrows indicate cytoskeletal extensions/attachment, blue arrows indicate regions with onset of degradation.

Figure 12. alamarBlue™ assay of the unloaded, TA loaded and TGF-β1 loaded scaffolds (B1-B8) against MC3T3 cell line. Error bars represents mean ± SD (n=3), *p<0.05, **p<0.01, ***p<0.001, ****p<0.0001.

Figure 13. Live/dead assay of MC3T3 cells on the scaffolds (B1-B8) after 3 days. Scale bars represent 200 micrometers

Figure 14. Anti-inflammatory effect of the TA loaded scaffold against inflammatory mediator TNF-α (A) and IL-6 (B). Error bars represents mean ± SD (n=3), * = p<0.05.

Figure 15. Osteogenic effect of the TA loaded scaffolds against bone markers RUNX2 (A) and ALP (B). Error bars represents mean ± SD (n=3), * = p<0.05.

Scheme 1:

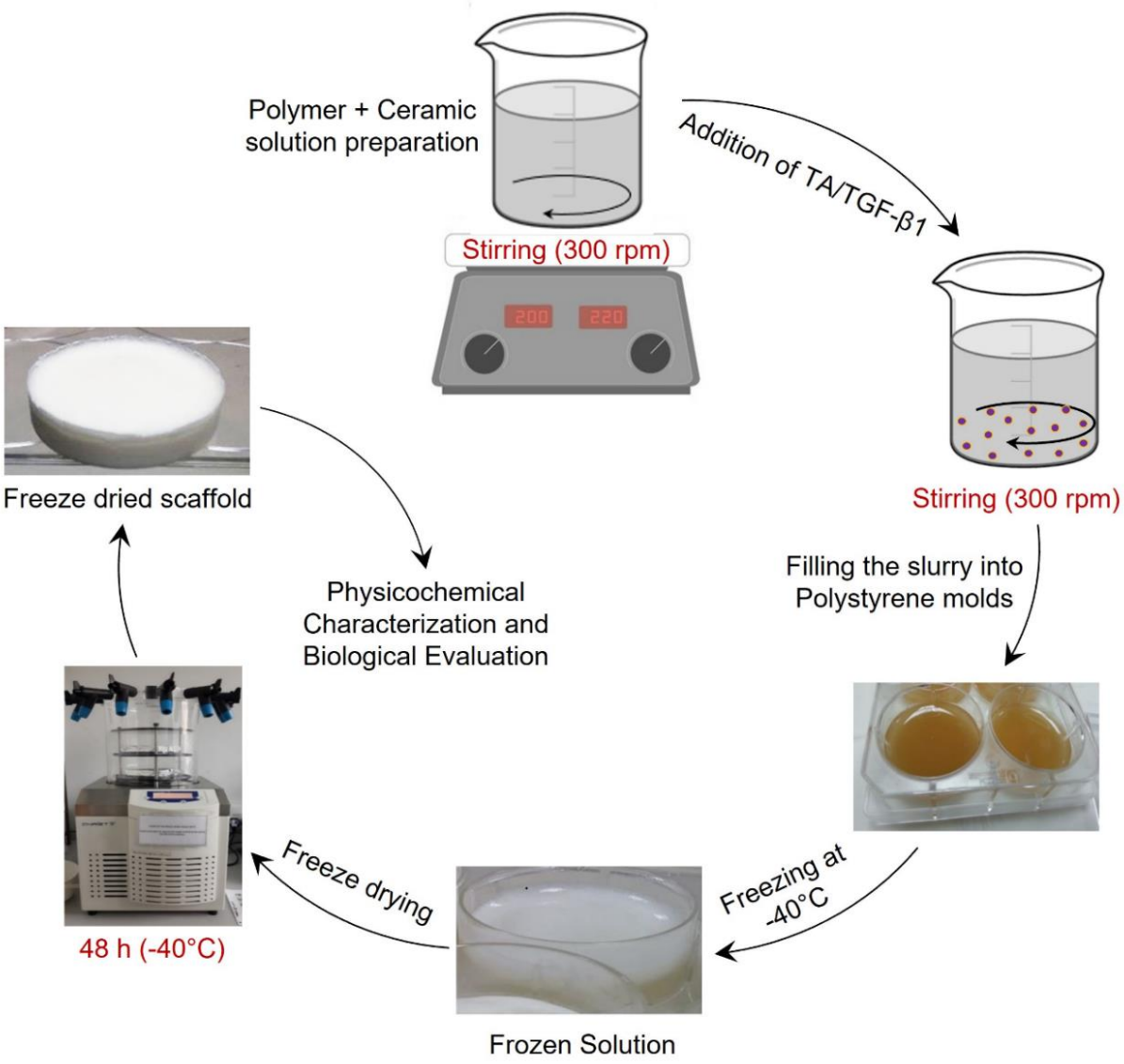
Polymer + Ceramic solution preparation
Stirring (300 rpm)
Addition of TA/TGF-β1
Stirring (300 rpm)
Filling the slurry into Polystyrene molds
Freezing at -40°C
Frozen Solution
Freeze drying
48 h (-40°C)
Physicochemical Characterization and Biological Evaluation
Freeze dried scaffold

Figure 1:

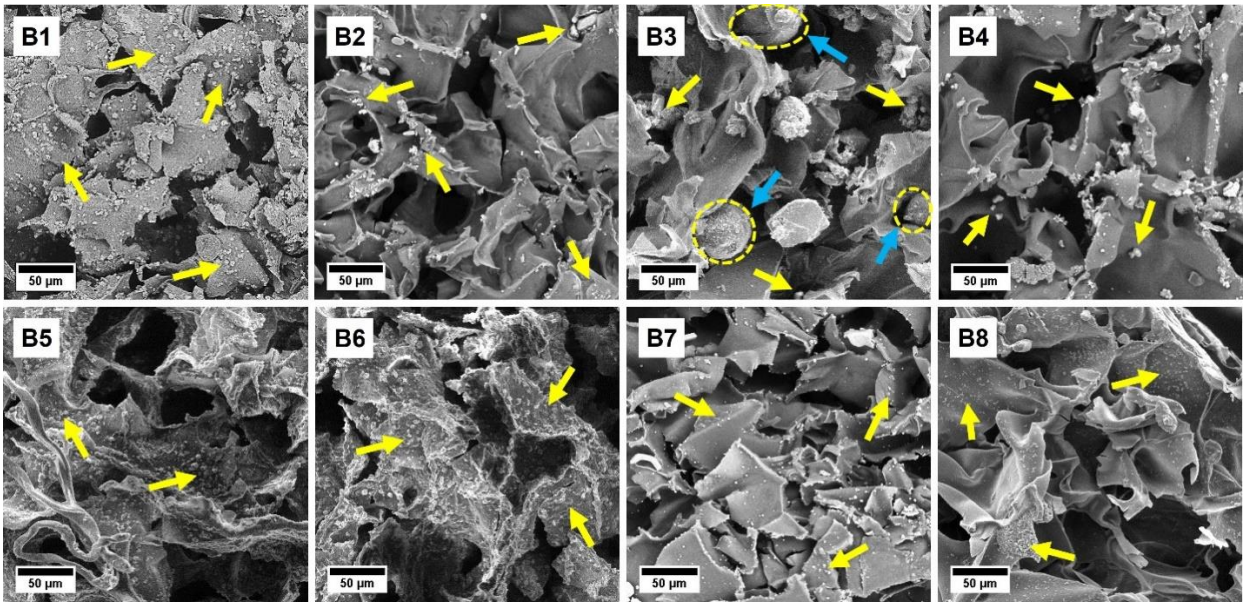

Figure 2:

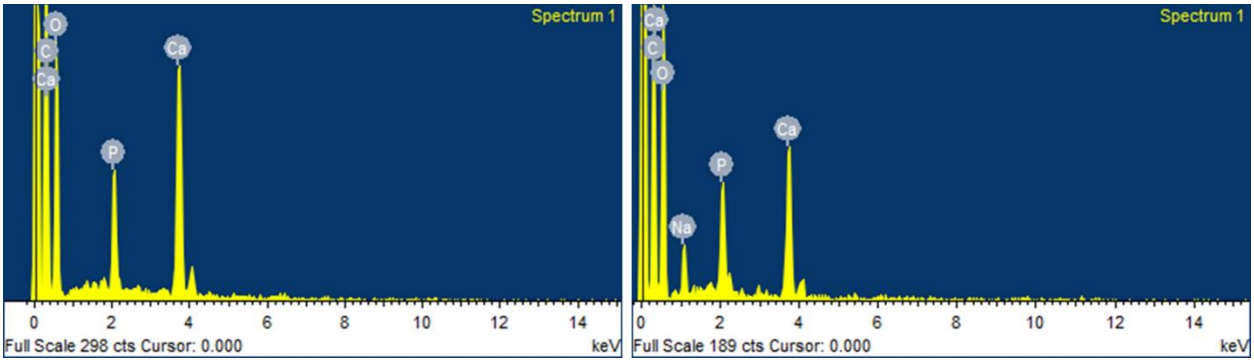
Spectrum 1
O
C
Ca
Ca
P
0
2
4
6
8
10
12
14
Full Scale 298 cts Cursor: 0.000
keV
Spectrum 1
Ca
C
O
Ca
P
Na
0
2
4
6
8
10
12
14
Full Scale 189 cts Cursor: 0.000
keV

Figure 3:

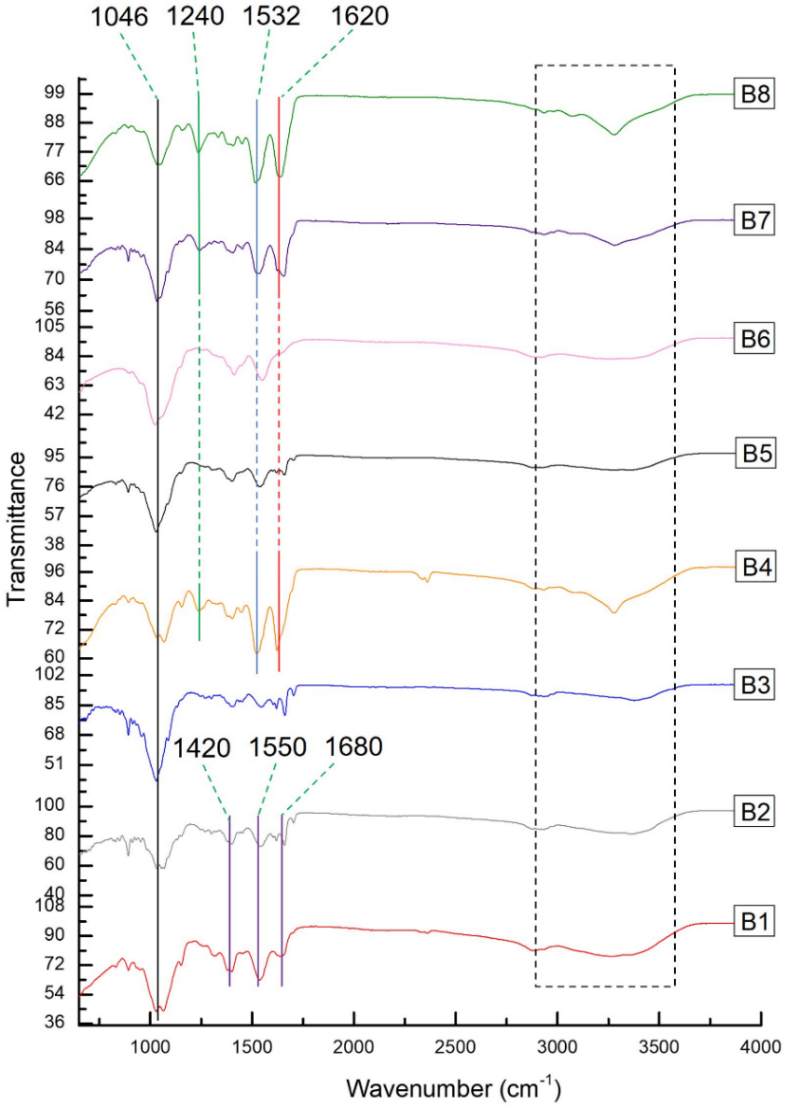
1046
1240
1532
1620
1420
1550
1680
B8
B7
B6
B5
B4
B3
B2
B1
Transmittance
Wavenumber (cm-1)
1000
1500
2000
2500
3000
3500
4000

Figure 4:

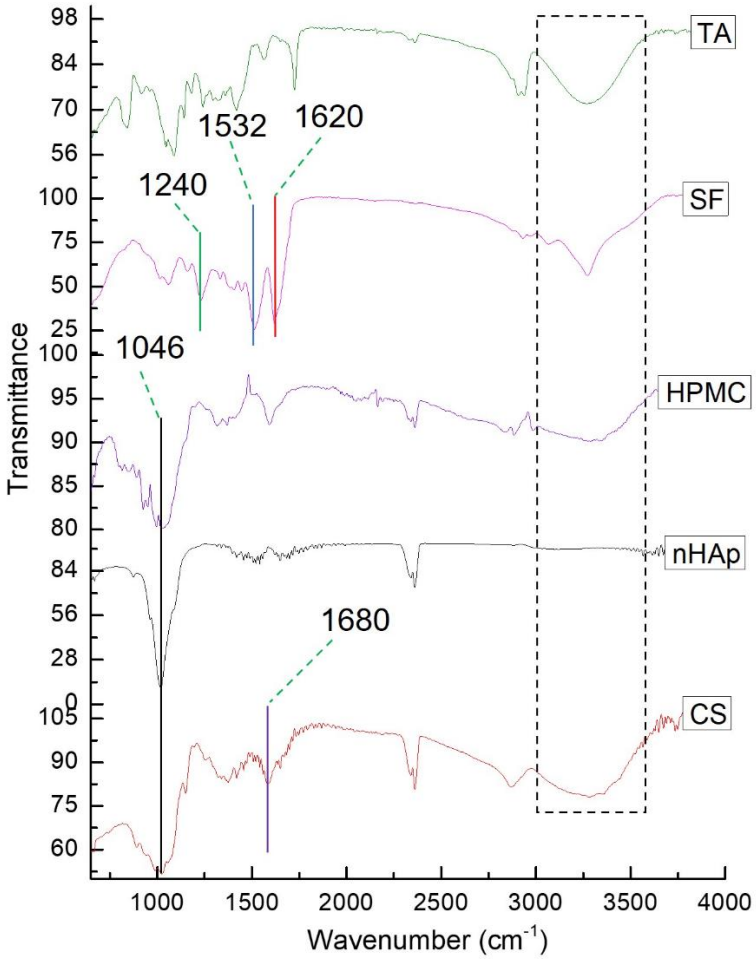
TA
SF
HPMC
nHAp
CS
1532
1620
1240
1046
1680
Transmittance
Wavenumber (cm-1)

Figure 5:

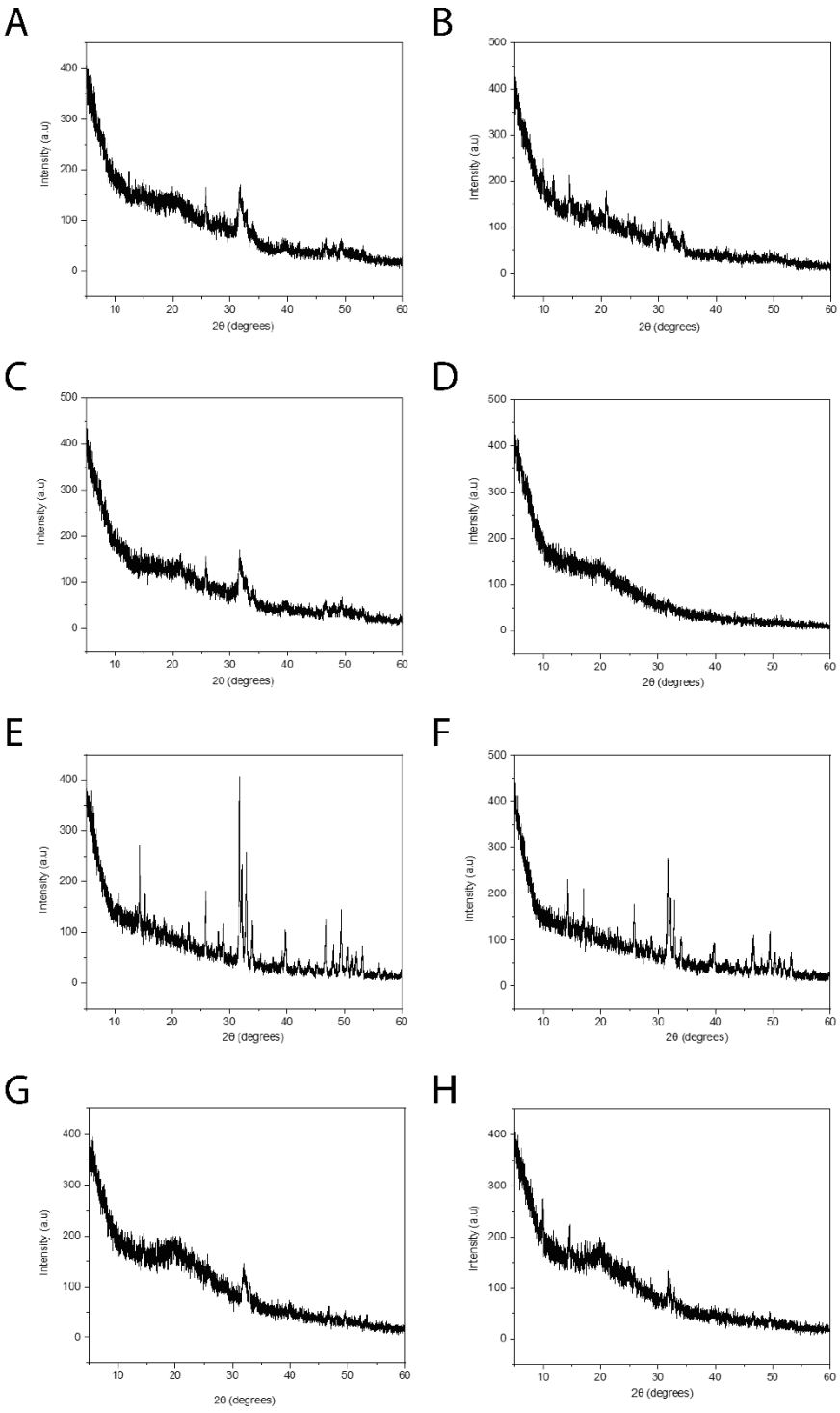

Figure 6:

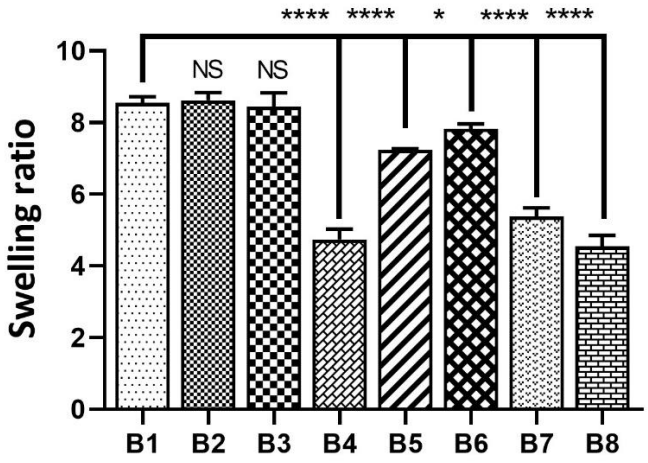

Figure 7:

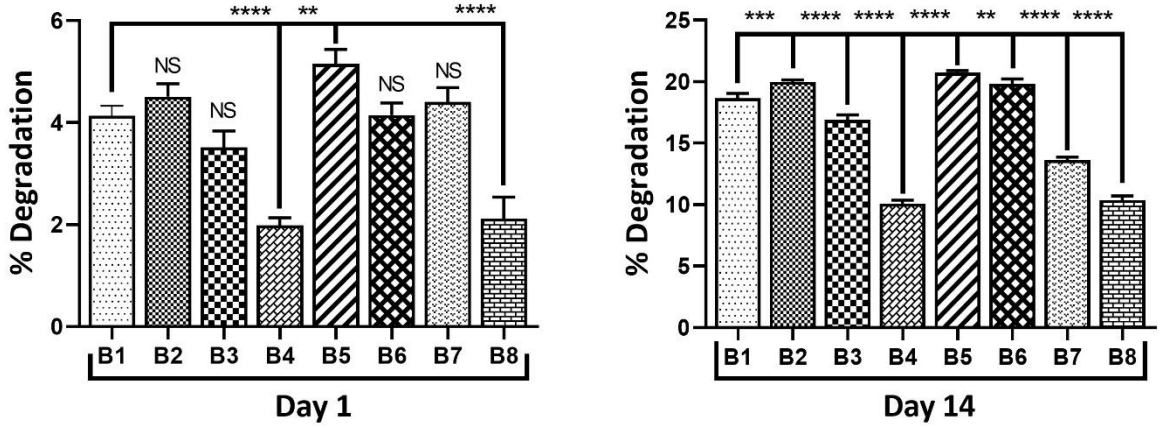
% Degradation
6
4
2
0
NS
NS
NS
****
**
****
B1
B2
B3
B4
B5
B6
B7
B8
Day 1
% Degradation
25
20
15
10
5
0
***
****
****
****
**
****
****
B1
B2
B3
B4
B5
B6
B7
B8
Day 14

Figure 8:

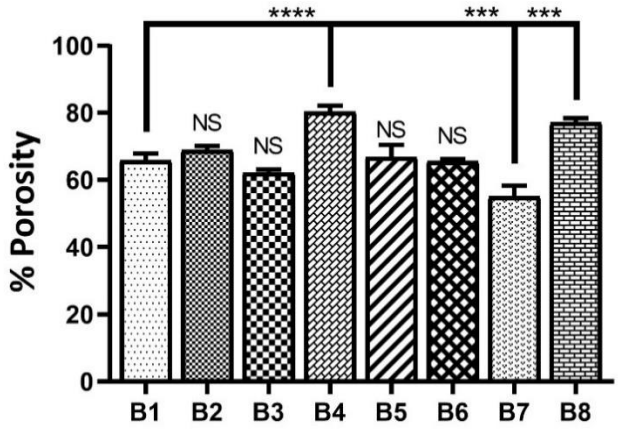

Figure 9:

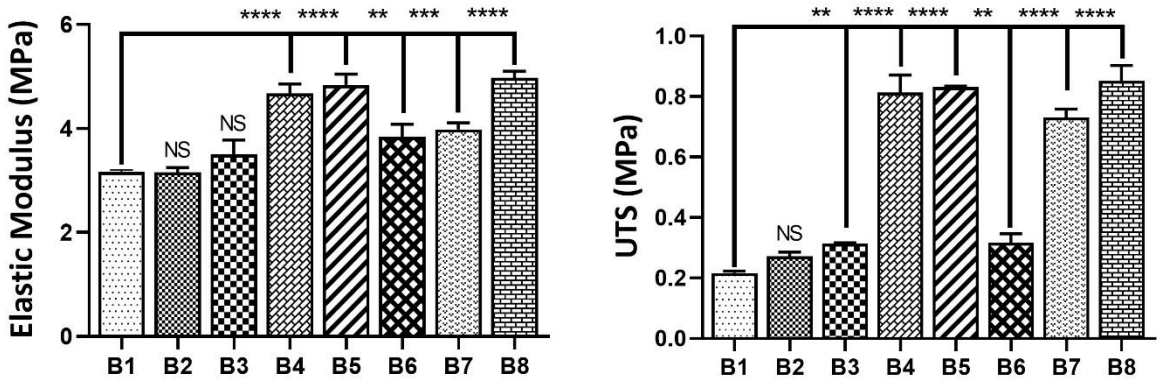
Elastic Modulus (MPa)
6
4
2
0
**** **** ** *** ****
NS
NS
B1 B2 B3 B4 B5 B6 B7 B8
UTS (MPa)
1.0
0.8
0.6
0.4
0.2
0.0
** **** **** ** **** ****
NS
B1 B2 B3 B4 B5 B6 B7 B8

Figure 10:

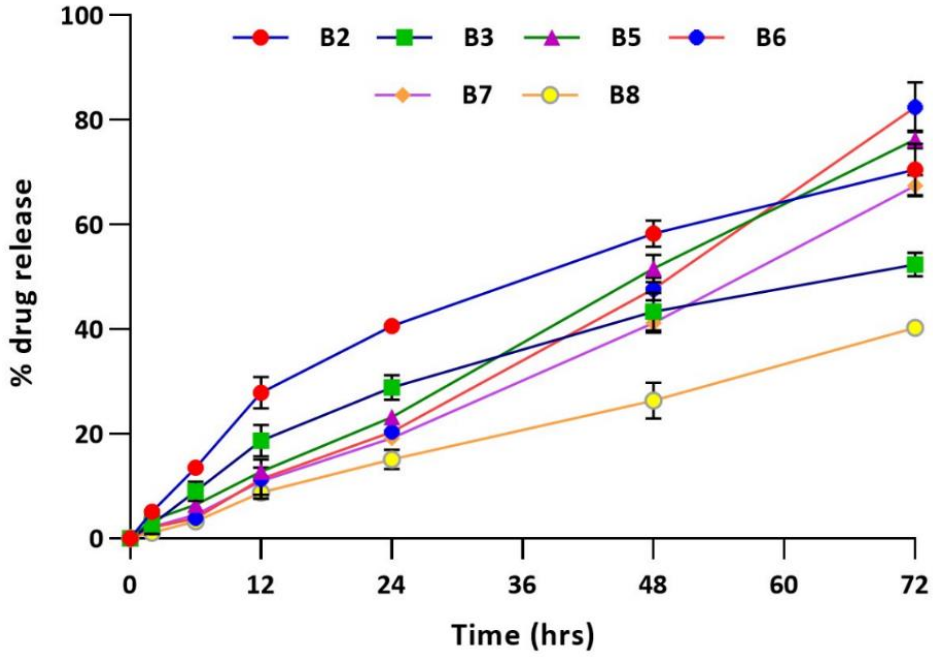
B2
B3
B5
B6
B7
B8
% drug release
Time (hrs)
0
20
40
60
80
100
0
12
24
36
48
60
72

Figure 11:

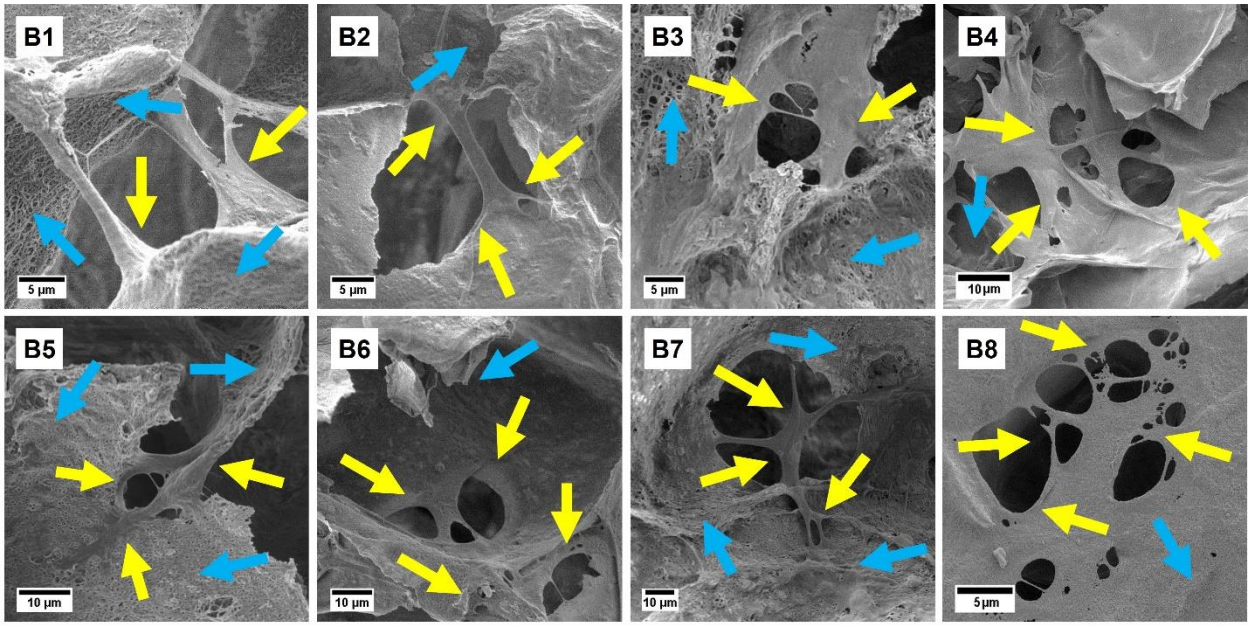

Figure 12:

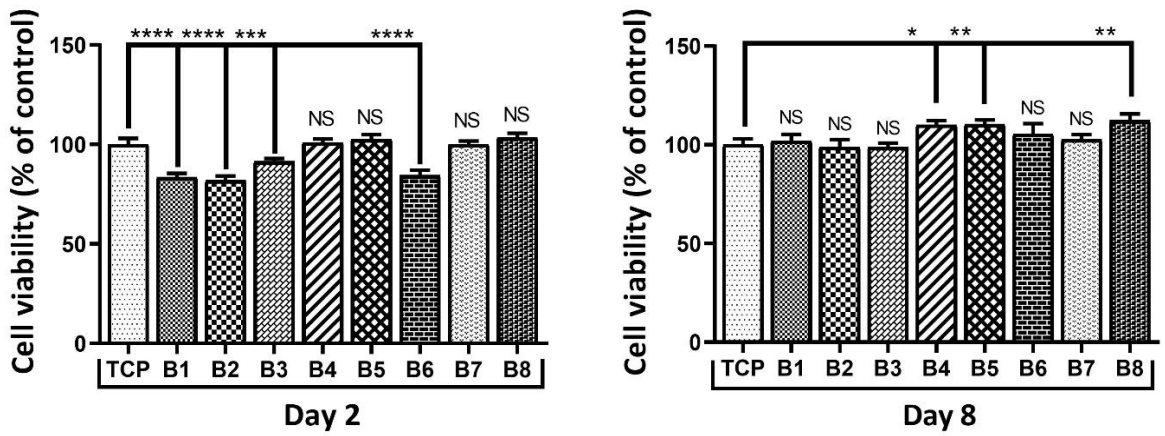
Cell viability (% of control)
150
100
50
0
**** **** *** ****
NS NS NS NS
TCP B1 B2 B3 B4 B5 B6 B7 B8
Day 2
Cell viability (% of control)
150
100
50
0
* ** **
NS NS NS NS NS
TCP B1 B2 B3 B4 B5 B6 B7 B8
Day 8

Figure 13:

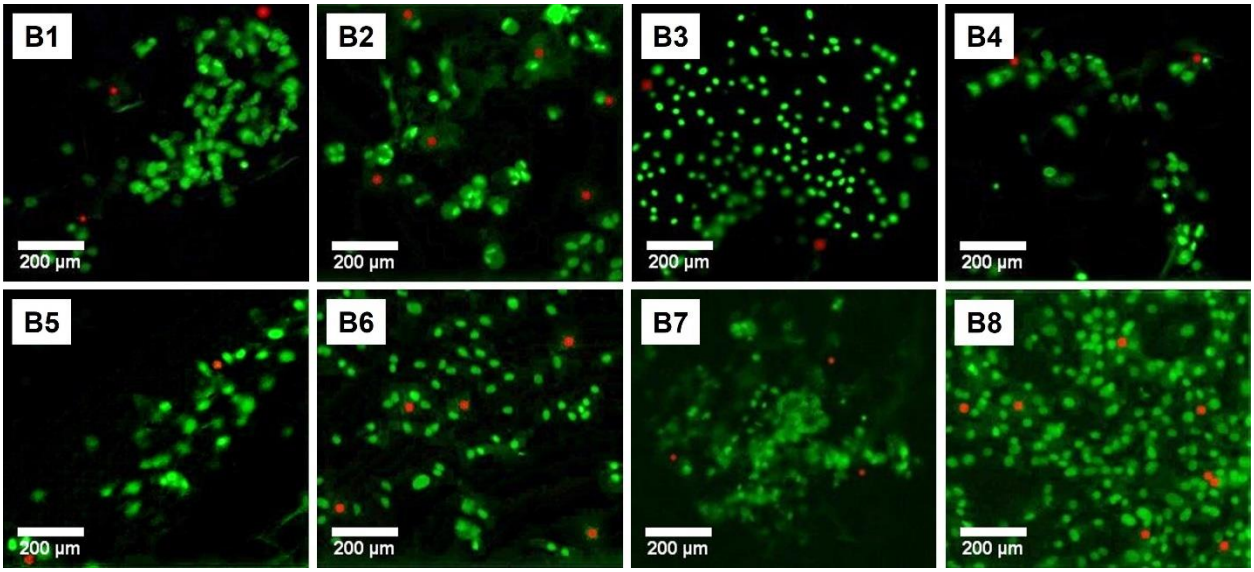
B1
200 µm
B2
200 µm
B3
200 µm
B4
200 µm
B5
200 µm
B6
200 µm
B7
200 µm
B8
200 µm

Figure 14:

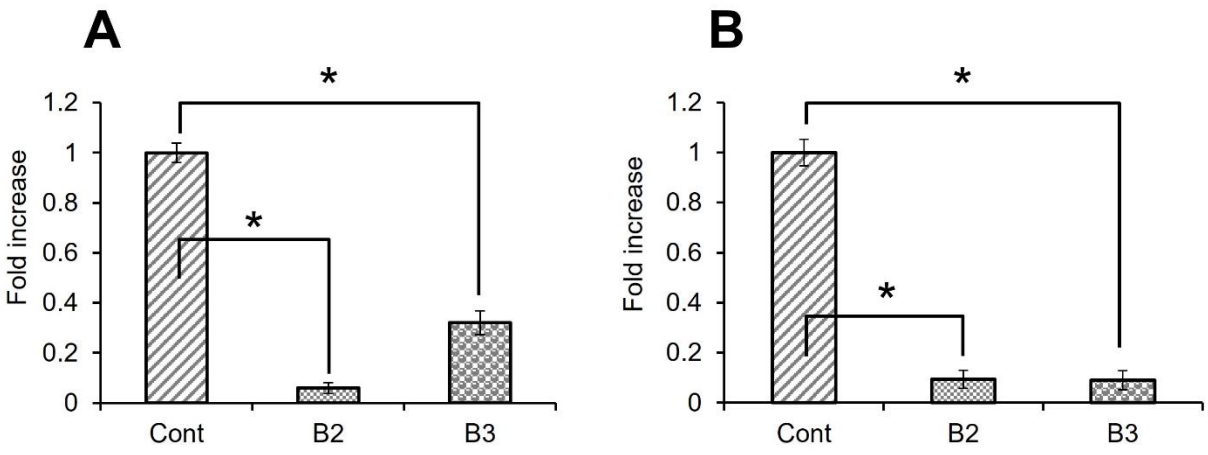

Figure 15:

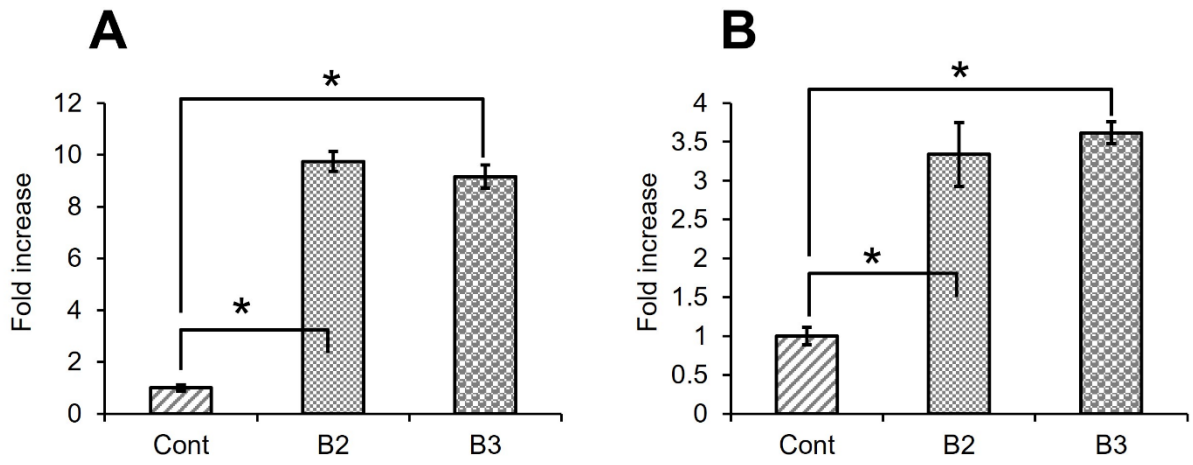

References

[1] N.L. Grimm, J.M. Weiss, J.I. Kessler, S.K. Aoki, Osteochondritis dissecans of the knee: pathoanatomy, epidemiology, and diagnosis, Clin. Sports Med. 33 (2014) 181-188, https://doi.org/10.1016/j.csm.2013.11.006

[2] M. Howell, Q. Liao, C.W. Gee, Surgical Management of Osteochondral Defects of the Knee: An Educational Review, Curr. Rev. Musculoskelet. Med. 14 (2021) 60-66, https://doi.org/10.1007/s12178-020-09685-1

[3] H. Pereira, I.F. Cengiz, C. Vilela, P.L. Ripoll, J. Espregueira-Mendes, J. Miguel Oliveira, R.L. Reis, C. Niek van Dijk, Emerging Concepts in Treating Cartilage, Osteochondral Defects, and Osteoarthritis of the Knee and Ankle, in: J.M. Oliveira, S. Pina, R.L. Reis, J. San Roman (Eds.), Osteochondral Tissue Engineering: Challenges, Current Strategies, and Technological Advances, Springer International Publishing, Cham, 2018, pp. 25-62.

[4] G.C. Gracitelli, V.Y. Moraes, C.E. Franciozi, M.V. Luzo, J.C. Belloti, Surgical interventions (microfracture, drilling, mosaicplasty, and allograft transplantation) for treating isolated cartilage defects of the knee in adults, Cochrane Database Syst. Rev. (2016), https://doi.org/10.1002/14651858.CD010675.pub2

[5] K.T.A. Lambers, J. Dahmen, M.L. Reilingh, C.J.A. van Bergen, S.A.S. Stufkens, G.M.M.J. Kerkhoffs, No superior surgical treatment for secondary osteochondral defects of the talus, Knee Surg. Sports Traumatol. Arthrosc. 26 (2018) 2158-2170, https://doi.org/10.1007/s00167-017-4629-0

[6] G. Smedslund, I. Kjeken, F. Musial, J. Sexton, N. Østerås, Interventions for osteoarthritis pain: A systematic review with network meta-analysis of existing Cochrane reviews, Osteoarthr. Cartil. 4 (2022) 100242, https://doi.org/10.1016/j.ocarto.2022.100242

[7] D. Seow, Y. Yasui, I.D. Hutchinson, E.T. Hurley, Y. Shimozono, J.G. Kennedy, The Subchondral Bone Is Affected by Bone Marrow Stimulation: A Systematic Review of Preclinical Animal Studies, Cartilage 10 (2017) 70-81, https://doi.org/10.1177/1947603517711220

[8] A.H. Gomoll, H. Madry, G. Knutsen, N. van Dijk, R. Seil, M. Brittberg, E. Kon, The subchondral bone in articular cartilage repair: current problems in the surgical management, Knee Surg. Sports Traumatol. Arthrosc. 18 (2010) 434-447, https://doi.org/10.1007/s00167-010-1072-x

[9] P. Orth, H. Madry, Advancement of the subchondral bone plate in translational models of osteochondral repair: implications for tissue engineering approaches, Tissue Eng. Part B: Rev. 21 (2015) 504-520, https://doi.org/10.1089/ten.teb.2015.0122

[10] J. Anita Lett, S. Sagadevan, I. Fatimah, M.E. Hoque, Y. Lokanathan, E. Léonard, S.F. Alshahateet, R. Schirhagl, W.C. Oh, Recent advances in natural polymer-based hydroxyapatite scaffolds: Properties and applications, Eur. Polym. J. 148 (2021) 110360, https://doi.org/10.1016/j.eurpolymj.2021.110360

[11] J. Fan, K. Abedi-Dorcheh, A. Sadat Vaziri, F. Kazemi-Aghdam, S. Rafieyan, M. Sohrabinejad, M. Ghorbani, F. Rastegar Adib, Z. Ghasemi, K. Klavins, V. Jahed, A Review of Recent Advances in Natural Polymer-Based Scaffolds for Musculoskeletal Tissue Engineering, Polymers 14 (2022) 2097, https://doi.org/10.3390/polym14102097

[12] R. Ferracini, I. Martínez Herreros, A. Russo, T. Casalini, F. Rossi, G. Perale, Scaffolds as structural tools for bone-targeted drug delivery, Pharmaceutics 10 (2018) 122, https://doi.org/10.3390/pharmaceutics10030122

[13] F. Gao, Z. Xu, Q. Liang, B. Liu, H. Li, Y. Wu, Y. Zhang, Z. Lin, M. Wu, C. Ruan, W. Liu, Direct 3D Printing of High Strength Biohybrid Gradient Hydrogel Scaffolds for Efficient Repair of Osteochondral Defect, Adv. Funct. Mater. 28 (2018) 1706644, https://doi.org/10.1002/adfm.201706644
[14] H. Madry, A. Rey-Rico, J.K. Venkatesan, B. Johnstone, M. Cucchiarini, Transforming growth factor beta-releasing scaffolds for cartilage tissue engineering, Tissue Eng. Part B: Rev. 20 (2014) 106-125, https://doi.org/10.1089/ten.teb.2013.0271
[15] R. Longley, A.M. Ferreira, P. Gentile, Recent approaches to the manufacturing of biomimetic multi-phasic scaffolds for osteochondral regeneration, Int. J. Mol. Sci. 19 (2018) 1755, https://doi.org/10.3390/ijms19061755
[16] G. Bauza-Mayol, M. Quintela, A. Brozovich, M. Hopson, S. Shaikh, F. Cabrera, A. Shi, F.B. Niclot, F. Paradiso, E. Combellack, T. Jovic, P. Rees, E. Tasciotti, L.W. Francis, P. Mcculloch, F. Taraballi, Biomimetic Scaffolds Modulate the Posttraumatic Inflammatory Response in Articular Cartilage Contributing to Enhanced Neoformation of Cartilaginous Tissue In Vivo, Adv. Healthc. Mater. 11 (2022) 2101127, https://doi.org/10.1002/adhm.202101127
[17] M. Domenech, L. Polo-Corrales, J.E. Ramirez-Vick, D.O. Freytes, Tissue Engineering Strategies for Myocardial Regeneration: Acellular Versus Cellular Scaffolds? , Tissue Eng. Part B: Rev. 22 (2016) 438-458, https://doi.org/10.1089/ten.teb.2015.0523
[18] S. Jiang, M. Wang, J. He, A review of biomimetic scaffolds for bone regeneration: Toward a cell-free strategy, Bioeng. Transl. Med. 6 (2021) e10206, https://doi.org/10.1002/btm2.10206
[19] Y. Liu, L. Peng, L. Li, C. Huang, K. Shi, X. Meng, P. Wang, M. Wu, L. Li, H. Cao, 3D-bioprinted BMSC-laden biomimetic multiphasic scaffolds for efficient repair of osteochondral defects in an osteoarthritic rat model, Biomaterials 279 (2021) 121216, https://doi.org/10.1016/j.biomaterials.2021.121216
[20] P. Abdollahiyan, F. Oroojalian, A. Mokhtarzadeh, M. de la Guardia, Hydrogel-Based 3D Bioprinting for Bone and Cartilage Tissue Engineering, Biotechnol. J. 15 (2020) 2000095, https://doi.org/10.1002/biot.202000095
[21] A.C. Daly, F.E. Freeman, T. Gonzalez-Fernandez, S.E. Critchley, J. Nulty, D.J. Kelly, 3D Bioprinting for Cartilage and Osteochondral Tissue Engineering, Adv. Healthc. Mater. 6 (2017) 1700298, https://doi.org/10.1002/adhm.201700298
[22] J.-N. Fu, X. Wang, M. Yang, Y.-R. Chen, J.-Y. Zhang, R.-H. Deng, Z.-N. Zhang, J.-K. Yu, F.-Z. Yuan, Scaffold-Based Tissue Engineering Strategies for Osteochondral Repair, Front. Bioeng. Biotechnol. 9 (2022), https://doi.org/10.3389/fbioe.2021.812383
[23] N.R. Richbourg, N.A. Peppas, V.I. Sikavitsas, Tuning the biomimetic behavior of scaffolds for regenerative medicine through surface modifications, J. Tissue Eng. Regen. Med. 13 (2019) 1275-1293, https://doi.org/10.1002/term.2859
[24] S. Wu, X. Liu, K.W.K. Yeung, C. Liu, X. Yang, Biomimetic porous scaffolds for bone tissue engineering, Mater. Sci. Eng. R Rep. 80 (2014) 1-36, https://doi.org/10.1016/j.mser.2014.04.001
[25] R.J. Hickey, A.E. Pelling, Cellulose Biomaterials for Tissue Engineering, Front. Bioeng. Biotechnol. 7 (2019), https://doi.org/10.3389/fbioe.2019.00045
[26] S.M. Ahsan, M. Thomas, K.K. Reddy, S.G. Sooraparaju, A. Asthana, I. Bhatnagar, Chitosan as biomaterial in drug delivery and tissue engineering, Int. J. Biol. Macromol. 110 (2018) 97-109, https://doi.org/10.1016/j.ijbiomac.2017.08.140
[27] W. Sun, D.A. Gregory, M.A. Tomeh, X. Zhao, Silk fibroin as a functional biomaterial for tissue engineering, Int. J. Mol. Sci. 22 (2021) 1499, https://doi.org/10.3390/ijms22031499

[28] D.R. Sahoo, T. Biswal, Alginate and its application to tissue engineering, SN Appl. Sci. 3 (2021) 1-19, https://doi.org/10.1007/s42452-020-04096-w
[29] T.J. Levingstone, A. Matsiko, G.R. Dickson, F.J. O'Brien, J.P. Gleeson, A biomimetic multi-layered collagen-based scaffold for osteochondral repair, Acta Biomater. 10 (2014) 1996-2004, https://doi.org/10.1016/j.actbio.2014.01.005
[30] G. Narayanan, V.N. Vernekar, E.L. Kuyinu, C.T. Laurencin, Poly (lactic acid)-based biomaterials for orthopaedic regenerative engineering, Adv. Drug Del. Rev. 107 (2016) 247-276, https://doi.org/10.1016/j.addr.2016.04.015
[31] R. Dwivedi, S. Kumar, R. Pandey, A. Mahajan, D. Nandana, D.S. Katti, D. Mehrotra, Polycaprolactone as biomaterial for bone scaffolds: Review of literature, J. Oral Biol. Craniofacial Res. 10 (2020) 381-388, https://doi.org/10.1016/j.jobcr.2019.10.003
[32] E.S. Place, J.H. George, C.K. Williams, M.M. Stevens, Synthetic polymer scaffolds for tissue engineering, Chem. Soc. Rev. 38 (2009) 1139-1151, https://doi.org/10.1039/B811392K
[33] Z. Terzopoulou, A. Zamboulis, I. Koumentakou, G. Michailidou, M.J. Noordam, D.N. Bikiaris, Biocompatible Synthetic Polymers for Tissue Engineering Purposes, Biomacromolecules 23 (2022) 1841-1863, https://doi.org/10.1021/acs.biomac.2c00047
[34] S. Liu, S. Qin, M. He, D. Zhou, Q. Qin, H. Wang, Current applications of poly(lactic acid) composites in tissue engineering and drug delivery, Compos. B. Eng 199 (2020) 108238, https://doi.org/10.1016/j.compositesb.2020.108238
[35] M. Wasyłeczko, W. Sikorska, A. Chwojnowski, Review of Synthetic and Hybrid Scaffolds in Cartilage Tissue Engineering, Membranes 10 (2020) 348, https://doi.org/10.3390/membranes10110348
[36] M. Samie, A.F. Khan, J.G. Hardy, M.A. Yameen, Electrospun Antibacterial Composites for Cartilage Tissue Engineering, Macromol. Biosci. n/a (2022) 2200219, https://doi.org/10.1002/mabi.202200219
[37] L. Zou, Y. Zhang, X. Liu, J. Chen, Q. Zhang, Biomimetic mineralization on natural and synthetic polymers to prepare hybrid scaffolds for bone tissue engineering, Colloids Surf. B. Biointerfaces 178 (2019) 222-229, https://doi.org/10.1016/j.colsurfb.2019.03.004
[38] C. Dai, Y. Li, W. Pan, G. Wang, R. Huang, Y. Bu, X. Liao, K. Guo, F. Gao, Three-Dimensional High-Porosity Chitosan/Honeycomb Porous Carbon/Hydroxyapatite Scaffold with Enhanced Osteoinductivity for Bone Regeneration, ACS Biomater. Sci. Eng. 6 (2020) 575-586, https://doi.org/10.1021/acsbiomaterials.9b01381
[39] Y. Li, X. Zhang, C. Dai, Y. Yin, L. Gong, W. Pan, R. Huang, Y. Bu, X. Liao, K. Guo, F. Gao, Bioactive Three-Dimensional Graphene Oxide Foam/Polydimethylsiloxane/Zinc Silicate Scaffolds with Enhanced Osteoinductivity for Bone Regeneration, ACS Biomater. Sci. Eng. 6 (2020) 3015-3025, https://doi.org/10.1021/acsbiomaterials.9b01931
[40] S. Bag, Biodegradable Composite Scaffold for Bone Tissue Regeneration, in: S. Paul (Ed.), Biomedical Engineering and its Applications in Healthcare, Springer Singapore, Singapore, 2019, pp. 657-679.
[41] M.S. Islam, M. Abdulla-Al-Mamun, A. Khan, M. Todo, Excellency of Hydroxyapatite Composite Scaffolds for Bone Tissue Engineering, in: Petrică Vizureanu, C.M.D.C.F. Botelho (Eds.), Biomaterials, IntechOpen2020, pp. 53-73.
[42] M. Filippi, G. Born, M. Chaaban, A. Scherberich, Natural Polymeric Scaffolds in Bone Regeneration, Front. Bioeng. Biotechnol. 8 (2020) 474, https://doi.org/10.3389/fbioe.2020.00474
[43] M. Petretta, A. Gambardella, M. Boi, M. Berni, C. Cavallo, G. Marchiori, M.C. Maltarello, D. Bellucci, M. Fini, N. Baldini, Composite scaffolds for bone tissue regeneration based on PCL

and Mg-containing bioactive glasses, Biology 10 (2021) 398, https://doi.org/10.3390/biology10050398
[44] M. Dumont, R. Villet, M. Guirand, A. Montembault, T. Delair, S. Lack, M. Barikosky, A. Crepet, P. Alcouffe, F. Laurent, L. David, Processing and antibacterial properties of chitosan-coated alginate fibers, Carbohydr. Polym. 190 (2018) 31-42, https://doi.org/10.1016/j.carbpol.2017.11.088
[45] C. Martínez-Mora, A. Mrowiec, E.M. García-Vizcaíno, A. Alcaraz, J.L. Cenis, F.J. Nicolás, Fibroin and sericin from Bombyx mori silk stimulate cell migration through upregulation and phosphorylation of c-Jun, PLoS One 7 (2012) e42271, https://doi.org/10.1371/journal.pone.0042271
[46] H. Yamada, Y. Igarashi, Y. Takasu, H. Saito, K. Tsubouchi, Identification of fibroin-derived peptides enhancing the proliferation of cultured human skin fibroblasts, Biomaterials 25 (2004) 467-472, https://doi.org/10.1016/S0142-9612(03)00540-4
[47] J.H. Choi, D.K. Kim, J.E. Song, J.M. Oliveira, R.L. Reis, G. Khang, Silk Fibroin-Based Scaffold for Bone Tissue Engineering, in: H.J. Chun, K. Park, C.-H. Kim, G. Khang (Eds.), Novel Biomaterials for Regenerative Medicine, Springer Singapore, Singapore, 2018, pp. 371-387.
[48] R. LogithKumar, A. KeshavNarayan, S. Dhivya, A. Chawla, S. Saravanan, N. Selvamurugan, A review of chitosan and its derivatives in bone tissue engineering, Carbohydr. Polym. 151 (2016) 172-188, https://doi.org/10.1016/j.carbpol.2016.05.049
[49] J.G. Hardy, T.R. Scheibel, Composite materials based on silk proteins, Prog. Polym. Sci. 35 (2010) 1093-1115, https://doi.org/10.1016/j.progpolymsci.2010.04.005
[50] C. Ai, Y.H.D. Lee, X.H. Tan, S.H.S. Tan, J.H.P. Hui, J.C.-H. Goh, Osteochondral tissue engineering: Perspectives for clinical application and preclinical development, J. Orthop. Translat 30 (2021) 93-102, https://doi.org/10.1016/j.jot.2021.07.008
[51] P. Morouço, C. Fernandes, W. Lattanzi, Challenges and Innovations in Osteochondral Regeneration: Insights from Biology and Inputs from Bioengineering toward the Optimization of Tissue Engineering Strategies, J. Funct. Biomater. 12 (2021) 17, https://doi.org/10.3390/jfb12010017
[52] C. Vyas, H. Mishbak, G. Cooper, C. Peach, R.F. Pereira, P. Bartolo, Biological perspectives and current biofabrication strategies in osteochondral tissue engineering, Biomanuf. rev. 5 (2020) 2, https://doi.org/10.1007/s40898-020-00008-y
[53] S.-J. Seo, C. Mahapatra, R.K. Singh, J.C. Knowles, H.-W. Kim, Strategies for osteochondral repair: Focus on scaffolds, J. Tissue Eng. 5 (2014), https://doi.org/10.1177/2041731414541850
[54] Z. Julier, A.J. Park, P.S. Briquez, M.M. Martino, Promoting tissue regeneration by modulating the immune system, Acta Biomater. 53 (2017) 13-28, https://doi.org/10.1016/j.actbio.2017.01.056
[55] M. Li, H. Yin, Z. Yan, H. Li, J. Wu, Y. Wang, F. Wei, G. Tian, C. Ning, H. Li, C. Gao, L. Fu, S. Jiang, M. Chen, X. Sui, S. Liu, Z. Chen, Q. Guo, The immune microenvironment in cartilage injury and repair, Acta Biomater. 140 (2022) 23-42, https://doi.org/10.1016/j.actbio.2021.12.006
[56] W. Wang, L. Sun, P. Zhang, J. Song, W. Liu, An anti-inflammatory cell-free collagen/resveratrol scaffold for repairing osteochondral defects in rabbits, Acta Biomater. 10 (2014) 4983-4995, https://doi.org/10.1016/j.actbio.2014.08.022
[57] M. Kapoor, J. Martel-Pelletier, D. Lajeunesse, J.-P. Pelletier, H. Fahmi, Role of proinflammatory cytokines in the pathophysiology of osteoarthritis, Nat. Rev. Rheumatol. 7 (2011) 33-42, https://doi.org/10.1038/nrrheum.2010.196

[58] H. Newman, Y.V. Shih, S. Varghese, Resolution of inflammation in bone regeneration: From understandings to therapeutic applications, Biomaterials 277 (2021) 121114, https://doi.org/10.1016/j.biomaterials.2021.121114
[59] M.A. Wesdorp, S. Capar, Y.M. Bastiaansen-Jenniskens, N. Kops, L.B. Creemers, J.A.N. Verhaar, G.J.V.M. Van Osch, W. Wei, Intra-articular Administration of Triamcinolone Acetonide in a Murine Cartilage Defect Model Reduces Inflammation but Inhibits Endogenous Cartilage Repair, Am. J. Sports Med. 50 (2022) 1668-1678, https://doi.org/10.1177/03635465221083693
[60] C. Wernecke, H.J. Braun, J.L. Dragoo, The effect of intra-articular corticosteroids on articular cartilage: a systematic review, Orthop. J. Sports Med. 3 (2015), https://doi.org/10.1177/2325967115581163
[61] M. Siebelt, N. Korthagen, W. Wei, H. Groen, Y. Bastiaansen-Jenniskens, C. Müller, J.H. Waarsing, M. de Jong, H. Weinans, Triamcinolone acetonide activates an anti-inflammatory and folate receptor–positive macrophage that prevents osteophytosis in vivo, Arthrit. Res. Ther. 17 (2015) 352, https://doi.org/10.1186/s13075-015-0865-1
[62] J. Paik, S.T. Duggan, S.J. Keam, Triamcinolone Acetonide Extended-Release: A Review in Osteoarthritis Pain of the Knee, Drugs 79 (2019) 455-462, https://doi.org/10.1007/s40265-019-01083-3
[63] I. Rudnik-Jansen, K. Schrijver, N. Woike, A. Tellegen, S. Versteeg, P. Emans, G. Mihov, J. Thies, N. Eijkelkamp, M. Tryfonidou, L. Creemers, Intra-articular injection of triamcinolone acetonide releasing biomaterial microspheres inhibits pain and inflammation in an acute arthritis model, Drug Deliv. 26 (2019) 226-236, https://doi.org/10.1080/10717544.2019.1568625
[64] M.N. Ferrao Blanco, Y.M. Bastiaansen Jenniskens, N. Kops, A. Chavli, R. Narcisi, S.M. Botter, P.J.M. Leenen, G.J.V.M. van Osch, N. Fahy, Intra-articular injection of triamcinolone acetonide sustains macrophage levels and aggravates osteophytosis during degenerative joint disease in mice, Br. J. Pharmacol. 179 (2022) 2771-2784, https://doi.org/10.1111/bph.15780
[65] J.-P. Liang, R.P. Accolla, K. Jiang, Y. Li, C.L. Stabler, Controlled Release of Anti-Inflammatory and Proangiogenic Factors from Macroporous Scaffolds, Tissue Eng. Part A 27 (2021) 1275-1289, https://doi.org/10.1089/ten.tea.2020.0287
[66] C.L. Huang, W.L. Lee, J.S.C. Loo, Drug-eluting scaffolds for bone and cartilage regeneration, Drug Discov. Today 19 (2014) 714-724, https://doi.org/10.1016/j.drudis.2013.11.007
[67] P.J. Kondiah, P.P. Kondiah, Y.E. Choonara, T. Marimuthu, V. Pillay, A 3D bioprinted pseudo-bone drug delivery scaffold for bone tissue engineering, Pharmaceutics 12 (2020) 166, https://doi.org/10.3390/pharmaceutics12020166
[68] J.Y. Park, S.H. Park, M.G. Kim, S.-H. Park, T.H. Yoo, M.S. Kim, Biomimetic Scaffolds for Bone Tissue Engineering, in: I. Noh (Ed.), Biomimetic Medical Materials: From Nanotechnology to 3D Bioprinting, Springer Singapore, Singapore, 2018, pp. 109-121.
[69] M. Samie, M.A. Yameen, H.F. Ikram, H. Iqbal, A.A. Chaudhry, I. ur Rehman, A.F. Khan, Fabrication of dual drug loaded bilayered chitosan based composite scaffolds as osteochondral substitutes and evaluation of in vitro cell response using the MC3T3 pre-osteoblast cell line, Cellulose 27 (2020) 2253-2266, https://doi.org/10.1007/s10570-019-02915-x
[70] A. Ajisawa, Dissolution of silk fibroin with calciumchloride/ethanol aqueous solution Studies on the dissolution of silk fibroin.(IX), J. Seric. Sci. Jpn. 67 (1998) 91-94, https://doi.org/10.11416/kontyushigen1930.67.91
[71] Y. Ocal, B. Kurum, S. Karahan, A. Tezcaner, S. Ozen, D. Keskin, Characterization and evaluation of triamcinolone, raloxifene, and their dual-loaded microspheres as prospective local

treatment system in rheumatic rat joints, J. Pharm. Sci. 103 (2014) 2396-2405, https://doi.org/10.1002/jps.24058
[72] G.D. Porta, B.N.B. Nguyen, R. Campardelli, E. Reverchon, J.P. Fisher, Synergistic effect of sustained release of growth factors and dynamic culture on osteoblastic differentiation of mesenchymal stem cells, J Biomed Mater Res A 103 (2015) 2161-2171, https://doi.org/10.1002/jbm.a.35354
[73] M. Srikanth, R. Asmatulu, K. Cluff, L. Yao, Material characterization and bioanalysis of hybrid scaffolds of carbon nanomaterial and polymer nanofibers, ACS omega 4 (2019) 5044-5051, https://doi.org/10.1021/acsomega.9b00197
[74] X. Niu, Y. Wei, Q. Liu, B. Yang, N. Ma, Z. Li, L. Zhao, W. Chen, D. Huang, Silver-loaded microspheres reinforced chitosan scaffolds for skin tissue engineering, Eur. Polym. J. 134 (2020) 109861, https://doi.org/10.1016/j.eurpolymj.2020.109861
[75] N. Bhardwaj, S.C. Kundu, Silk fibroin protein and chitosan polyelectrolyte complex porous scaffolds for tissue engineering applications, Carbohydr. Polym. 85 (2011) 325-333, https://doi.org/10.1016/j.carbpol.2011.02.027
[76] M.A. Nazeer, O.C. Onder, I. Sevgili, E. Yilgor, I.H. Kavakli, I. Yilgor, 3D printed poly (lactic acid) scaffolds modified with chitosan and hydroxyapatite for bone repair applications, Mater. Today Commun. 25 (2020) 101515, https://doi.org/10.1016/j.mtcomm.2020.101515
[77] A.C. Akman, R. Seda Tığlı, M. Gümüşderelioğlu, R.M. Nohutcu, Bone Morphogenetic Protein-6-loaded Chitosan Scaffolds Enhance the Osteoblastic Characteristics of MC3T3-E1 Cells, Artif. Organs 34 (2010) 65-74, https://doi.org/10.1111/j.1525-1594.2009.00798.x
[78] A. Sionkowska, M. Michalska-Sionkowska, M. Walczak, Preparation and characterization of collagen/hyaluronic acid/chitosan film crosslinked with dialdehyde starch, Int. J. Biol. Macromol. 149 (2020) 290-295, https://doi.org/10.1016/j.ijbiomac.2020.01.262
[79] S.P. Uswatta, I.U. Okeke, A. Jayasuriya, Injectable porous nano-hydroxyapatite/chitosan/tripolyphosphate scaffolds with improved compressive strength for bone regeneration, Mater. Sci. Eng., C 69 (2016) 505-512, https://doi.org/10.1016/j.msec.2016.06.089
[80] B. Yetiskin, O. Okay, High-strength and self-recoverable silk fibroin cryogels with anisotropic swelling and mechanical properties, Int. J. Biol. Macromol. 122 (2019) 1279-1289, https://doi.org/10.1016/j.ijbiomac.2018.09.087
[81] D. Li, G. Jiao, W. Zhang, X. Chen, R. Ning, C. Du, Hybrid scaffolding strategy for dermal tissue reconstruction: a bioactive glass/chitosan/silk fibroin composite, RSC advances 6 (2016) 19887-19896, https://doi.org/10.1039/C5RA26871K
[82] K. Maji, S. Dasgupta, K. Pramanik, A. Bissoyi, Preparation and evaluation of gelatin-chitosan-nanobioglass 3D porous scaffold for bone tissue engineering, Int. J. Biomater. 2016 (2016), https://doi.org/10.1155/2016/9825659
[83] H.R. Fernandes, A. Gaddam, A. Rebelo, D. Brazete, G.E. Stan, J.M.F. Ferreira, Bioactive Glasses and Glass-Ceramics for Healthcare Applications in Bone Regeneration and Tissue Engineering, Materials 11 (2018) 2530, https://doi.org/10.3390/ma11122530
[84] N. Abbasi, S. Hamlet, R.M. Love, N.-T. Nguyen, Porous scaffolds for bone regeneration, Journal of Science: Advanced Materials and Devices 5 (2020) 1-9, https://doi.org/10.1016/j.jsamd.2020.01.007
[85] X. Wang, S. Xu, S. Zhou, W. Xu, M. Leary, P. Choong, M. Qian, M. Brandt, Y.M. Xie, Topological design and additive manufacturing of porous metals for bone scaffolds and orthopaedic implants: A review, Biomaterials 83 (2016) 127-141, https://doi.org/10.1016/j.biomaterials.2016.01.012

[86] Z. Wang, S. Hou, S. Yao, Y. Shang, S. Deng, Y. Peng, W. Zhou, X. Lv, B. Ren, C. Peng, J. Yang, Z. Huang, Osteogenesis of aspirin microsphere-loaded tilapia collagen/hydroxyapatite biomimetic scaffolds, J. Mater. Sci. 57 (2022) 11882-11898, https://doi.org/10.1007/s10853-022-07368-5
[87] J.G. Hardy, L.M. Römer, T.R. Scheibel, Polymeric materials based on silk proteins, Polymer 49 (2008) 4309-4327, https://doi.org/10.1016/j.polymer.2008.08.006
[88] Z. Zhou, Q. Yao, L. Li, X. Zhang, B. Wei, L. Yuan, L. Wang, Antimicrobial activity of 3D-printed poly (ε-caprolactone)(PCL) composite scaffolds presenting vancomycin-loaded polylactic acid-glycolic acid (PLGA) microspheres, Med. Sci. Monit. 24 (2018) 6934, https://doi.org/10.12659/MSM.911770
[89] L. Wang, C. Wang, S. Wu, Y. Fan, X. Li, Influence of the mechanical properties of biomaterials on degradability, cell behaviors and signaling pathways: current progress and challenges, Biomat. Sci. 8 (2020) 2714-2733, https://doi.org/10.1039/D0BM00269K
[90] H. Jodati, B. Yılmaz, Z. Evis, A review of bioceramic porous scaffolds for hard tissue applications: Effects of structural features, Ceram. Int. 46 (2020) 15725-15739, https://doi.org/10.1016/j.ceramint.2020.03.192
[91] E. Bahremandi-Toloue, Z. Mohammadalizadeh, S. Mukherjee, S. Karbasi, Incorporation of inorganic bioceramics into electrospun scaffolds for tissue engineering applications: A review, Ceram. Int. 48 (2022) 8803-8837, https://doi.org/10.1016/j.ceramint.2021.12.125
[92] A.R. Shrivats, M.C. McDermott, J.O. Hollinger, Bone tissue engineering: state of the union, Drug Discov. Today 19 (2014) 781-786, https://doi.org/10.1016/j.drudis.2014.04.010
[93] G. Singh, A. Chanda, Mechanical properties of whole-body soft human tissues: a review, Biomedical Materials 16 (2021) 062004, https://doi.org/10.1088/1748-605x/ac2b7a